Long-range spin coherence in a strongly coupled all-electronic dot-cavity system

Michael Sven Ferguson,[1] David Oehri,[1] Clemens Rössler,[2] Thomas Ihn,[3] Klaus Ensslin,[3]
Gianni Blatter,[1] and Oded Zilberberg[1]

[1]*Institute for Theoretical Physics, ETH Zurich, 8093 Zürich, Switzerland*
[2]*Infineon Technologies Austria, Siemensstraße 2, 9500 Villach, Austria*
[3]*Solid State Physics Laboratory, ETH Zurich, 8093 Zürich, Switzerland*

(Received 29 May 2017; revised manuscript received 30 October 2017; published 21 December 2017)

We present a theoretical analysis of spin-coherent electronic transport across a mesoscopic dot-cavity system. Such spin-coherent transport has been recently demonstrated in an experiment with a dot-cavity hybrid implemented in a high-mobility two-dimensional electron gas [C. Rössler *et al.*, Phys. Rev. Lett. **115**, 166603 (2015)] and its spectroscopic signatures have been interpreted in terms of a competition between Kondo-type dot-lead and molecular-type dot-cavity singlet formation. Our analysis brings forward all the transport features observed in the experiments and supports the claim that a spin-coherent molecular singlet forms across the full extent of the dot-cavity device. Our model analysis includes (i) a single-particle numerical investigation of the two-dimensional geometry, its quantum-coral–type eigenstates, and associated spectroscopic transport features, (ii) the derivation of an effective interacting model based on the observations of the numerical and experimental studies, and (iii) the prediction of transport characteristics through the device using a combination of a master-equation approach on top of exact eigenstates of the dot-cavity system, and an equation-of-motion analysis that includes Kondo physics. The latter provides additional temperature scaling predictions for the many-body phase transition between molecular- and Kondo-singlet formation and its associated transport signatures.

DOI: 10.1103/PhysRevB.96.235431

I. INTRODUCTION

Mesoscopic physics provides a framework for the study of coherent transport across engineered controllable systems. A standard method for obtaining such quantum coherent devices is by geometrically confining electrons to effectively low-dimensional structures that are embedded within ultra-clean materials. Typical devices include quantum dots acting as effectively zero-dimensional (0D) artificial atoms, one-dimensional (1D) quantum wires or quantum point contacts (QPC), and electronic interferometers composed of edges of two-dimensional (2D) quantum Hall bars [1]. In such devices, electron-electron interactions play an important role, giving way to numerous interesting transport phenomena, such as the Coulomb blockade [2] and the Kondo resonance [3,4] in quantum dots, the 0.7 conductance plateau in quantum point contacts [5–8], and noise signatures of fractionally charged particles in electronic interferometers [9–11].

Of particular interest in the present context are 2D coherent standing waves (quantum corrals) that have led to the observation of fascinating signatures of coherence and interaction. For example, a QPC coupled to a mesoscopic, μm-size quantum corral displays a modulated tunneling [12,13], while the observed Kondo mirage [14–17] is the result of nm-scale coherence and interaction. Such geometry-induced complex many-body phenomena can be described theoretically. When doing so, it is important to account for both the spatial structure of the electronic wave functions imposed by the device geometry as well as interactions.

In search for new phenomena and applications, the coupling of various mesoscopic devices has led to new implications on both fundamental questions in many-body physics as well as novel quantum engineering prospects. Examples of the former include the study of many-body quantum phase transitions in the context of the Kondo effect and competing mechanisms, such as Ruderman-Kittel-Kasuya-Yoshida (RKKY) interactions [18], two-channel Kondo [19], and singlet-triplet switching on a molecule [20]. On the engineering front, the combination of several dots into controlled quantum bits (qubits) has been demonstrated [21,22], thus promoting the next challenge of introducing coherent coupling between distant qubits without relying on nearest-neighbor exchange.

Recently, we have reported on the transport signatures of a coherent electronic dot-cavity system in a high-mobility two-dimensional electron gas [23]. The role of the (μm-size) cavity was played by a carefully designed electron reservoir of suitable geometrical shape, similar to that used in mesoscopic quantum corrals [12,13]. The high quality of the underlying material has allowed for the demonstration of a coherent spin-singlet formation that spans across the dot and extended cavity states. This strong hybridization between dot and cavity has quenched the competing Kondo transport in a controlled way, thus allowing for a systematic tuning of the device. Such strong hybridization typically occurs in quantum optics between photons and atoms when the optical cavities have a high-quality factor [24]; quite interestingly, we have seen it transpire for an electronic cavity that has a mere quality factor of $\sim$5. This highlights the important difference between the electronic and optical platforms: electrons are strongly interacting and the dot-cavity physics takes place within a many-body interacting Fermi sea of electrons, whereas photons are weakly interacting and optical cavities have isolated spectral lines.

In this paper, we provide a detailed account of the theoretical modeling invoked in the analysis of the dot-cavity experiments [23]. The work involves analytical and numerical studies of the 2D geometry that has facilitated the design of an optimized quality factor for the electronic cavity. Feeding

the spectral properties of the 2D structure into an effective 0D model (coupled to Fermi leads) allows us to introduce electron-electron interaction into the problem and describe the dot-cavity hybrid as an original realization of a Kondo-box setup [25–28]. We then employ several methods for the prediction of transport signatures associated with the effective model: we make use of a combination of exact-diagonalization, master-equation, and equation-of-motion approaches in order to analyze the complex many-body signatures observed in the experiment. Moreover, we present a detailed comparison of our model's predictions with the reported experimental results, as well as with previously unpublished experimental findings. The agreement is remarkable, both when comparing equilibrium and out-of-equilibrium transport.

The paper is structured as follows: In Sec. II, we analyze the effects of the 2D geometry of our system on the single-particle transport across the device. In Sec. III, we discuss how this geometrical shaping can be accounted for within an effective model. The many-body transport properties of this model are studied using exact diagonalization and a master-equation approach in Sec. IV. Finally, we discuss the interplay between the dot-lead Kondo physics and the dot-cavity spin-singlet formation using an equation-of-motion approach in Sec. VI, followed by the conclusions and an outlook in Sec. VII.

II. CAVITY ENGINEERING

The interesting physics arising in the dot-cavity experiment [23] is the result of a deliberate structuring of the two-dimensional electron gas (2DEG). The geometrical confinement generates modes which are related to the standing electron waves discussed in the context of quantum corrals [17]. Here, we analyze the single-particle effects of shaping the potential landscape. We do this numerically by considering the transport through a quantum point contact in the presence of an electronic cavity. We shall see that the (numerically calculated) local density of states (LDOS) of the device is related to the eigenfunctions of the corresponding closed system, a half-disk quantum box with hard walls. This relation provides us with a simple understanding of the observed features and allows us to set up specific design rules for future devices. Additionally, this analysis serves as the foundation for the construction of the effective many-body Hamiltonian in Sec. III where the QPC will be replaced by a quantum dot.

We consider a QPC connecting two extended leads, one of which is structured by a mirror gate [see the inset of Fig. 1(a)]. Such a setup is known to modulate the transmission through the QPC by forming ballistic resonator modes [12,13,23]. We model this device using the numerical transport package KWANT [29]. This involves a discretization of the system using a fine square-lattice mesh. To model the QPC, we separate the 2DEG into two parts along the y axis, denoted as left (L) and right (R), by a large onsite potential leaving only a small channel connecting them. In the absence of the mirror gate, the transport between the two separated 2DEG parts shows the well-known conductance quantization steps [30,31] as a function of energy ω [see the red dashed line in Fig. 1(a) following the first quantization step]. The curved mirror and QPC gates are positioned symmetrically around the x axis and define a half-circular cavity for electrons which causes a

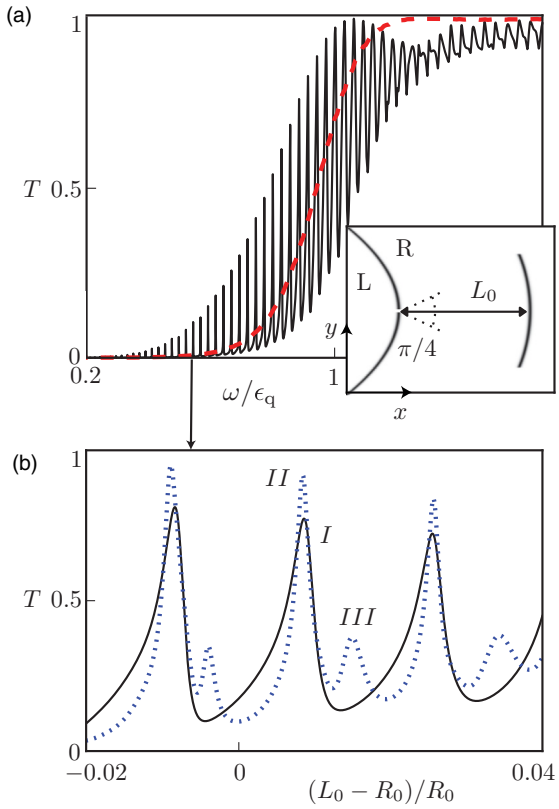

FIG. 1. Transmission modulation of a QPC due to a structured lead. The inset shows the geometry of the QPC-cavity setup used in our numerical simulation: two parts of the 2DEG (L and R) are separated by a potential barrier leaving only a narrow connecting channel that defines a QPC. At a distance L_0, we include a curved potential with radius R_0 and an opening angle $\pi/4$ (cavity mirror). (a) In the absence of the cavity mirror (dashed red line), the transmission T versus energy ω shows the expected conductance quantization, with an arbitrary quantization energy ϵ_q. In the presence of the $\pi/4$ cavity with $R_0 = L_0$ (solid line), the transmission is modulated by pronounced, well-separated resonances. (b) Transmission through the QPC at $\omega = 0.54\epsilon_q$ and fixed radius R_0 as a function of the cavity-mirror position L_0. The results of two mirror opening angles are presented, a narrow mirror with opening angle $\pi/4$ (solid line) and a wider mirror with opening angle $\pi/2$ (dotted blue line). The former shows a regular pattern of isolated resonances, while the latter shows main resonances accompanied by additional side resonances. For a larger distance from the QPC, the resonances become broader and less transmitting due to additional scattering into the surrounding lead. I, II, and III denote peaks in transmission for which the scattering single-particle states are depicted in Figs. 2(b)–2(d), respectively.

pronounced oscillation in the transmission through the QPC [see the solid line in Fig. 1(a)].

In the experiment, a gate voltage was applied to the mirror gate that reduced the length of the radial confinement of the cavity [23]. We model this by studying the transmission at a fixed energy ω as a function of the distance of the mirror from the QPC [see Fig. 1(b)]. We observe a regular pattern of resonances, in accord with the experiment. Increasing the opening angle from $\pi/4$ to $\pi/2$ shows additional resonances, demonstrating that the optimal cavity has to be carefully

tuned in order to arrive at well-separated but still sharp transport resonances. To better understand the properties of these resonances, we study the eigenstates in a closed half-disk quantum box that has a shape similar to that of the cavity. Indeed, these states are closely related to the resonances seen in an open microwave billiard [13].

We start with the eigenstates of a circular box with radius R_0, and work in both Cartesian x, y and circular r, φ coordinates, according to convenience. In circular coordinates, the Schrödinger equation for free particles is

$$\frac{1}{r}\frac{\partial}{\partial r}\left(r\frac{\partial\psi}{\partial r}\right)+\frac{1}{r^2}\frac{\partial^2\psi}{\partial\varphi^2}+k^2\psi=0. \tag{1}$$

Adding a circular confining potential generates eigenstates of the form $\psi_{n,\pm m}(\mathbf{r})\propto J_m(k_n r)e^{\pm im\varphi}$ with the cylindrical Bessel functions J_m and k_n the nth solution of $J_m(kR_0)=0$. The integers n and m are the radial and azimuthal quantum numbers, respectively. The solutions with $\pm m$ are energetically degenerate, such that arbitrary superpositions of them are solutions as well. The wave functions must vanish at the QPC gates, which lie on the y axis. For a given $|m|>0$, we can create superpositions which fulfill this criterion

$$\tilde{\psi}_{n,m}(\mathbf{r})\propto J_m(k_n r)\sin\left[m(\varphi+\pi/2)\right], \tag{2}$$

where we take $\varphi=0$ to lie on the x axis. These specific superpositions are eigenstates of the half-circular disk defined on $-\pi/2<\varphi<\pi/2$. A selection of such states is shown in Fig. 2(a).

We now consider how a wave incoming from the left of the QPC will tunnel into cavity states on the right-hand side. First, we establish a selection rule on m due to the parity of the initial and final wave functions. The incoming wave e^{ikx} is even under the sign change $y\to -y$ and hence scatters into states (2) with odd m. Second, due to the effective potential of high angular-momentum modes, the local density of states (LDOS) of the cavity eigenstates at the QPC is suppressed for large azimuthal quantum numbers m and, thus, they couple less strongly to the incoming wave. Hence, promising solutions that strongly couple across the QPC are modes with small odd values of m.

Inspiration for optimizing the cavity geometry to produce a strong and coherent dot-cavity coupling can be drawn from quantum electrodynamical (QED) setups [24]. We define the Q factor of our cavity to be the ratio of the peak-to-peak distance and the full width at half maximum (inverse lifetime) of the peaks. Reaching the strong coupling limit between a QED cavity photon and an atom requires a high-Q factor. In the electronic system, the cavity electron strongly interacts with the electrons on the quantum dot (artificial atom) and a moderate Q factor is sufficient. We can maximize the Q factor by optimizing the cavity geometry and applying the quantum engineering insights obtained above.

Our tuning parameters for the Q factor are then the lifetime of the states in the cavity and their distance in energy space. The lifetime highly depends on how well confined the states are and hence on the opening angle of the cavity mirror. If a large fraction of the weight of a state is located in a region which is not confined by the mirror gate, it will leak out very fast and thus the lifetime will be short, leading to broad resonances

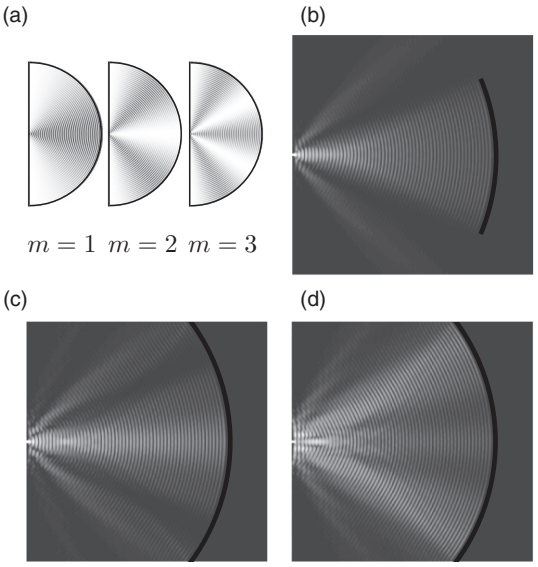

FIG. 2. Resonances of closed and open half-disks. (a) Eigenstates of a closed half-circular quantum box. Here, the modes with $n=40$ and $m=1,2,3$ are plotted [see Eq. (2)]. For clarity, we show the local density of states of the modes multiplied by the radius r, $r|\tilde{\psi}_{40,m}(\mathbf{r})|^2$. (b)–(d) The local density of states of a plane-wave scattering through the QPC into the structured lead as obtained using the numerical transport package KWANT [29]. In (b) and (c), we show the modes that lead to the pronounced resonances I and II in Fig. 1(b) of the narrow and wide mirrors, respectively. These modes both have angular quantum number $m=1$ and correspond to the same state in a closed system. Their respective resonances differ in height and width because the narrow mirror is less effective in confining the mode. In (d), we depict the LDOS corresponding to the side resonance III in Fig. 1(b) of the wide mirror with angular quantum number $m=3$.

when the opening angle of the cavity is small. On the other hand, a small cavity opening leads to the disappearance of high-m modes and thus the peak-to-peak distance increases. These features are illustrated in Fig. 1(b), where we see that the side peak with $m=3$ broadens and disappears when the cavity mirror is narrowed. Selected states corresponding to the peaks in transmission in Fig. 1(b) are pictured in Figs. 2(b)–2(d).

Thus, decreasing the opening angle of the cavity has two competing implications for Q: (i) high-m modes are not confined and therefore side peaks vanish such that Q increases, and (ii) the main $m=1$ mode broadens, decreasing the lifetime and thus Q. We find a cavity opening angle $\pi/4$ to be a good compromise between isolated and sharp resonances. A further analysis of the quality of the cavity depends on the exact shape of the gates, their relative sizes, and its robustness to disorder and is beyond the scope of this work.

In this section, we investigated the single-particle properties of the cavity. We found that when tuned correctly, the cavity acts as an effectively one-dimensional box coupled to a reservoir. We also showed that we can use analytic tools to provide design guidelines, and that KWANT [29] can function as a low-cost test bed for the design of future devices. In Sec. III, we will combine these results with the interacting quantum dot to create effective models for the entire device.

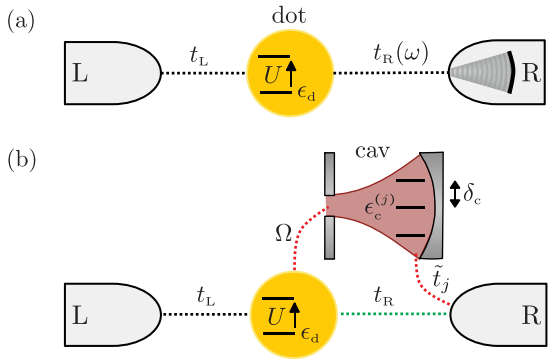

FIG. 3. Effective models describing the interacting dot-cavity system. (a) Anderson-type model where the effect of the structured lead is accounted for by an energy-dependent transmission coefficient $t_R(\omega)$ [see Eq. (7)]. (b) Dot-cavity model where the effect of the structured lead is accounted for by discrete cavity states separately coupled to the dot and to the right lead. Closed paths connecting the dot via the cavity to the right lead (red dotted lines) and back to the dot (green dotted) might generate Fano interference, however, the summation over such trajectories (see Fig. 4) will suppress this effect.

III. EFFECTIVE MODELS

Next, we set up an effective model for an interacting dot-cavity system, where we replace the QPC by an interacting quantum dot including its spin degree degree of freedom and include cavity states as discussed above. Given the large extent of the cavity, we assume that cavity charging effects are screened and thus can be ignored. The cavity modes are then assumed to solely affect the tunneling amplitude from the dot into a "structured" lead.

Our first model Hamiltonian describes the quantum dot in terms of an Anderson model with a standard (unstructured) coupling to the left lead and includes the cavity in terms of a structured right lead with an energy-dependent transmission coefficient [see Fig. 3(a)]

$$H = H_{\text{leads}} + H_{\text{dot}} + H_{\text{tun}}, \tag{3}$$

where

$$H_{\text{leads}} = \sum_{k,\sigma} \epsilon_{\text{L}k} c^\dagger_{\text{L}k\sigma} c_{\text{L}k\sigma} + \sum_{k,\sigma} \epsilon_{\text{R}k} c^\dagger_{\text{R}k\sigma} c_{\text{R}k\sigma} \tag{4}$$

describes the left and right leads with creation and annihilation operators of lead states $c^\dagger_{ak\sigma}$ and $c_{ak\sigma}$ with energy ϵ_{ak} and where σ and k denote spin and momenta of the states in the left (a = L) and right (a = R) leads. We consider a dot with a single spin-degenerate level as described by an Anderson model [32]

$$H_{\text{dot}} = \sum_\sigma \epsilon_{\text{d}} d^\dagger_\sigma d_\sigma + U n_\uparrow n_\downarrow, \tag{5}$$

with creation and annihilation operators $d^\dagger_\sigma$ and d_σ of the dot level with energy ϵ_{d} and spin σ, $n_\sigma = d^\dagger_\sigma d_\sigma$, and the onsite Coulomb interaction is denoted by U. The coupling between the leads and the dot is described by the tunneling Hamiltonian

$$H_{\text{tun}} = \sum_{k,\sigma} t_{\text{L}} d^\dagger_\sigma c_{\text{L}k\sigma} + \sum_{k,\sigma} t_{\text{R}}(\omega_k)\, d^\dagger_\sigma c_{\text{R}k\sigma} + \text{H.c.}, \tag{6}$$

where we assume a constant tunneling amplitude t_{L} between the left lead and the dot level and an *energy-dependent* tunneling amplitude $t_{\text{R}}(\omega)$ between the dot level and the right lead state with energy ω. The energies ω_k of the lead states are related to their momenta $\hbar k$ through the density of states $\rho = dk/d\omega_k$. The energy dependence of the tunneling amplitude to the right lead is given by the specific shape of the resonances in Fig. 1(a). This shape is well approximated by separated Lorentzian peaks on top of a constant background

$$t_{\text{R}}(\omega) = t_{\text{R}} + \sum_j \frac{\lambda_j}{\omega - \epsilon_{\text{c}}^{(j)} + i\Gamma_j/2}. \tag{7}$$

Here, the amplitude t_{R} describes the direct transmission from the dot to the right lead and the sum over Lorentzians accounts for the transmission into the right lead via the cavity states. The energy of the cavity resonances is given by $\epsilon_{\text{c}}^{(j)}$ while Γ_j and λ_j describe their width and coupling strength, respectively. Note that the analytic expression in Eq. (7) incorporates the effect of the cavity modes as resonances in the transmission coefficient. In doing so, we account for the cavity coherence in the right lead via a (large) finite lifetime $\hbar/\Gamma_j$, i.e., narrow resonances.

Second effective model. On the other hand, we can go one step further and describe these cavity states as discrete levels that are tunnel coupled to the dot and are broadened by tunnel coupling to the background states of the right lead. This setting is described by the Hamiltonian

$$\bar{H} = H_{\text{leads}} + H_{\text{dot}} + H_{\text{cav}} + H_{\text{coupl}} + \bar{H}_{\text{tun}}, \tag{8}$$

where the cavity Hamiltonian

$$H_{\text{cav}} = \sum_{\sigma,j} \epsilon_{\text{c}}^{(j)} f^\dagger_{j\sigma} f_{j\sigma} \tag{9}$$

describes the discrete cavity levels $\epsilon_{\text{c}}^{(j)}$ with creation and annihilation operators $f^\dagger_{j\sigma}$ and $f_{j\sigma}$, the coupling Hamiltonian

$$H_{\text{coupl}} = \sum_{j,\sigma} \Omega_j f^\dagger_{j\sigma} d_\sigma + \text{H.c.} \tag{10}$$

accounts for the coupling between the dot and cavity states, and the modified tunneling Hamiltonian

$$\begin{aligned}\bar{H}_{\text{tun}} &= H^{\text{dL}}_{\text{tun}} + \bar{H}^{\text{dR}}_{\text{tun}} + \bar{H}^{\text{cR}}_{\text{tun}} \\ &= \sum_{k,\sigma} (t_{\text{L}} d^\dagger_\sigma c_{\text{L}k\sigma} + \text{H.c.}) + \sum_{k,\sigma} (t_{\text{R}} d^\dagger_\sigma c_{\text{R}k\sigma} + \text{H.c.}) \\ &\quad + \sum_{j,k,\sigma} (t_j f^\dagger_{j\sigma} c_{\text{R}k\sigma} + \text{H.c.})\end{aligned} \tag{11}$$

describes the tunneling between both unstructured leads and the dot as well as the coupling of the cavity to the unstructured right lead. The tunneling amplitudes t_j that describe the coupling of the cavity levels to the right lead are related to the cavity resonance widths by [33] $\Gamma_j = 2\pi\rho_{\text{R}}|t_j|^2$, with ρ_{R} the density of states in the right lead. The hybridization amplitude $\Omega_j = \lambda_j/t_j$ between the dot and the cavity is related to the strength λ_j of the resonance and its width [33]. Similarly, the amplitudes t_{a} that couple the dot to the left (a = L) and right (a = R) leads give rise to rates

$$\Gamma_{\text{a}} = 2\pi\rho_{\text{a}}|t_{\text{a}}|^2, \tag{12}$$

that broaden the dot level.

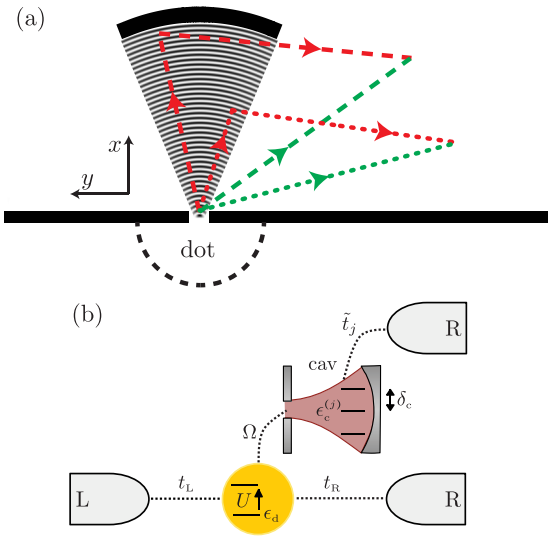

FIG. 4. Suppression of Fano interference. (a) Two examples of interfering paths from the dot to a structured lead. Each set of paths (dashed and dotted) shows interferences between a trajectory going directly from the dot into the lead (green lines) and a trajectory connecting to the lead via the cavity (red lines). All such trajectories starting and ending in the same points must be averaged over. This turns into a double averaging, first over the end point (red-green vertex) including the 2D extent of the lead and second over the (red-red) cavity vertices within the cavity area. This summation causes the phase to average out and eliminates any Fano effect in the dot-cavity device, in agreement with the experiment [23] where no such interference effects could be observed. (b) Effective 0D model (coupled to Fermi leads) accounting properly for the elimination of Fano resonances by independently coupling the dot and cavity to the right lead. Note the differences to Fig. 3(b) with the red-green loop connecting the dot, cavity, and reservoir; the latter is now replaced by two independent reservoirs.

In the following, we will consider a fixed cavity-level spacing δ_c, i.e., $\epsilon_c^{(j)} = \epsilon_c + j\,\delta_c$, and additionally assume that all cavity levels are tunnel coupled to the dot and leads with the same amplitudes $\Omega_j = \Omega$ and $t_j = t_c$, respectively. Correspondingly, the rates coupling the cavity levels to the right lead are identical, $\Gamma_j = \Gamma_c$ with

$$\Gamma_c = 2\pi\rho_R|t_c|^2. \tag{13}$$

As a result, the dot-lead Hamiltonian corresponds to a standard Anderson-model–type description of an interacting dot with tunneling into unstructured leads [32] and an additional energy-dependent channel due to tunneling via the cavity [see Fig. 3(b)]. Note that obtaining the Hamiltonian H from $\bar{H}$ corresponds to tracing out the effect of the cavity. Here, we have performed the opposite procedure and "gave birth" to the coherent electronic cavity physics.

No Fano interference. In general in model (8), both t_R and Ω_j may have an energy-dependent relative phase, which could give rise to Fano-type interferences [34]. Recalling our 2D geometry, we argue that the direct transmission into the right lead and the transmission via the cavity into the right lead are phase averaged [see Fig. 4(a)]. As a result, we conclude that these two processes do not interfere and that the Fano effect is suppressed. We therefore will make sure in the following to sum these terms incoherently by creating a second copy of the right lead [see Fig. 4(b)] and thereby neglect Fano-type processes, in contrast to previous Kondo-box analyses [27,28]. Following, we will use the model in Fig. 4(b) in Secs. IV and V. Within our discussion of the Kondo physics in Sec. VI, the two models are equivalent (as we drop Fano-type interference effects) and we will use the structured-lead formulation of Eq. (6) and Fig. 3(a).

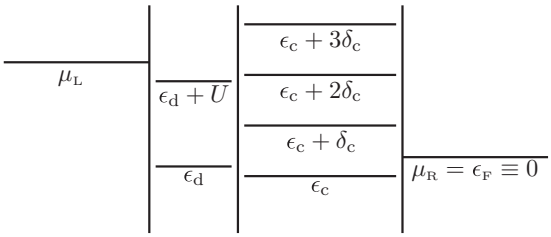

FIG. 5. Schematic view of the different tuning parameters in the dot-cavity system. We will investigate the effects of tuning the left chemical potential μ_L, the dot level ϵ_d, and the lowest cavity level ϵ_c, keeping the chemical potential μ_R in the right lead fixed. We use $\mu_R = 0$ as our zero of energy.

Transport configurations and capacitive cross talk. When analyzing the many-body properties of the Hamiltonian $\bar{H}$ in Eq. (8), we will study typical configurations as sketched in Fig. 5, with a fixed chemical potential $\mu_R = \epsilon_F$ on the right lead which we take as our zero of energy, $\mu_R = 0$. Transport across the device then is studied by changing the left chemical potential μ_L and tuning the dot ϵ_d and cavity ϵ_c levels. In addition, we assume a capacitive cross talk in the system between the dot and cavity such that

$$\epsilon_d = \epsilon_d' + \alpha_{cd}\epsilon_c' + \alpha_{Ld}\mu_L, \tag{14}$$

$$\epsilon_c = \epsilon_c' + \alpha_{dc}\epsilon_d', \tag{15}$$

where primed quantities ϵ_d' and ϵ_c' refer to applied gate voltages on the dot and cavity, respectively, producing the dot and cavity levels ϵ_d and ϵ_c in the Hamiltonian. The cross talks modify the diagrams through a global tilt and stretch; we seek only qualitatively correct values for the capacitive couplings and therefore use $\alpha_{cd} = 4\alpha_{dc} = 0.2$ and $\alpha_{Ld} = 0.5$, while quantitative values can be easily extracted from a proper calibration of the experiment.

IV. ARTIFICIAL DOT-CAVITY MOLECULE: AN EXACT DIAGONALIZATION TREATMENT

We study the many-body spinful interacting dot-cavity system coupled to leads as derived in Sec. III. Assuming that the coupling to the leads is weak relative to the dot-cavity coupling, we first analyze the (isolated) central region using exact diagonalization (ED) (see Sec. IV), and find the emergent "artificial molecule" ground-state map describing the isolated dot-cavity system. We find how this map changes as a function of various system parameters and compare it with a standard double-dot picture. We then couple the leads perturbatively to the dot-cavity artificial molecule and determine the linear

transport response across the device using a master-equation approach (see Sec. V). Signatures of Kondo transport are not captured by this formalism as we restrict the discussion to the lowest-order sequential transport. We will investigate Kondo physics in Sec. VI using an equation-of-motion approach.

Exact diagonalization: Ground-state map

The subsystem consisting of the dot and cavity is described by the Hamiltonian

$$H_{\rm dc} = H_{\rm dot} + H_{\rm cav} + H_{\rm coupl} \tag{16}$$

[see Eqs. (5), (9), and (10)]. Using exact diagonalization, we determine the eigenstates and eigenenergies of this isolated dot-cavity system. Specifically, for a fixed number $N^{\uparrow}$ of electrons with spin $\uparrow$ and $N^{\downarrow}$ electrons with spin $\downarrow$, we obtain the eigenstates $|\psi^{\alpha}_{N^{\uparrow},N^{\downarrow}}\rangle$ with the corresponding energies $\epsilon^{\alpha}_{N^{\uparrow},N^{\downarrow}}$, where α labels all eigenstates of this specific Fock space. These eigenstates can be written as a normalized superposition of the many-body occupation basis $|n_{\rm d}^{\uparrow},n_{\rm d}^{\downarrow},m_0^{\uparrow},m_0^{\downarrow},m_1^{\uparrow},m_1^{\downarrow},\ldots\rangle$,

$$\left|\psi^{\alpha}_{N^{\uparrow},N^{\downarrow}}\right\rangle = \sum_{n_{\rm d}^{\sigma}+\sum_j m_j^{\sigma}=N^{\sigma}} \mathcal{C}^{\alpha}_{n_{\rm d}^{\uparrow},n_{\rm d}^{\downarrow},m_0^{\uparrow},m_0^{\downarrow},m_1^{\uparrow},m_1^{\downarrow},\ldots} \times |n_{\rm d}^{\uparrow},n_{\rm d}^{\downarrow},m_0^{\uparrow},m_0^{\downarrow},m_1^{\uparrow},m_1^{\downarrow},\ldots\rangle, \tag{17}$$

where $n_{\rm d}^{\sigma}=0,1$ and $m_j^{\sigma}=0,1$ are the occupation numbers of the dot and jth cavity states with spin $\sigma=\uparrow,\downarrow$, respectively. We denote the lowest-energy eigenstate of each Fock sector with $\alpha=1$, i.e., $|\psi^{1}_{N^{\uparrow},N^{\downarrow}}\rangle$ is the state with $\epsilon^{1}_{N^{\uparrow},N^{\downarrow}} = \min_{\alpha}\epsilon^{\alpha}_{N^{\uparrow},N^{\downarrow}}$, while the remaining states $\alpha>1$ correspond to excited states.

When the system is coupled to a reservoir, the electron number is not fixed. Assuming that the system is weakly tunnel coupled to leads, $\Gamma_{\rm L},\Gamma_{\rm R},\Gamma_{\rm c} \ll \delta_{\rm c},U$, the leads populate the system in the ground state with $N^{\uparrow}$ and $N^{\downarrow}$ electrons. We can then go over to the addition spectrum representation [35] with energies $\tilde{\epsilon}_{\rm c}^{(j)} = \epsilon_{\rm c}^{(j)} - \epsilon_{\rm F}$ and $\tilde{\epsilon}_{\rm d} = \epsilon_{\rm d} - \epsilon_{\rm F}$ defined with respect to the chemical potential of the reservoir; with our choice $\epsilon_{\rm F}=0$, we have $\tilde{\epsilon}_{\rm c}^{(j)} = \epsilon_{\rm c}^{(j)}$ and $\tilde{\epsilon}_{\rm d} = \epsilon_{\rm d}$ and we drop the tilde in the following. The ground state then is given by the state with the lowest energy $\epsilon^{1}_{N^{\uparrow},N^{\downarrow}}$ as a function of filling $N^{\uparrow}$ and $N^{\downarrow}$. At vanishing bias $\mu_{\rm L}=0$, the open system will conduct when two neighboring Fock sectors have degenerate ground states that are also the ground states of the entire system. In such a configuration, an electron can be added to or removed from the artificial molecule through an energy-conserving process and, hence, the total particle number on the artificial molecule remains undetermined.

We can study the ground-state energies of different Fock sectors as a function of various system parameters: (i) the dot level $\epsilon_{\rm d}$, (ii) the onsite interaction on the dot U, (iii) the lowest-energy level of the cavity $\epsilon_{\rm c}$, (iv) the cavity-level spacing $\delta_{\rm c}$, and (v) the dot-cavity tunnel coupling Ω. We focus on the experimental situation [23], where the cavity-level spacing $\delta_{\rm c} \sim U \gg \Omega$. In this regime, the impact of the cavity is mostly due to a single one of its levels that is close to the chemical potential. In Fig. 6, we explore the dot particle-hole symmetric point $\epsilon_{\rm d} = -U/2$ and find that the degeneracy of the cavity level is lifted by a $12\,\Omega^2/U$ splitting (see Appendix A). In this

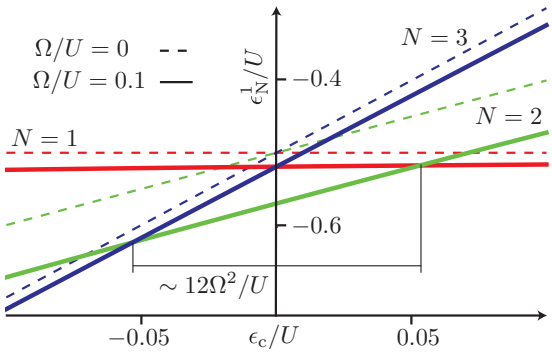

FIG. 6. Addition spectrum calculated through exact diagonalization. The ground-state energy of different Fock sectors ($N=1$, red; $N=2$, green; $N=3$, blue) is plotted as a function of the cavity level while the dot is in Coulomb blockade, $\epsilon_{\rm d} = -U/2$. All other Fock sectors are lifted further up in energy for this configuration. For vanishing temperature $T \to 0$ and infinitesimal coupling to the leads, the energetically lowest Fock sector is the one which will be occupied. Pushing the cavity level $\epsilon_{\rm c}$ across the Fermi level $\epsilon_{\rm F}$ from left to right entails its emptying $N=3 \to 2 \to 1$. The dashed lines describe the situation for a vanishing dot-cavity hopping Ω and show that the cavity occupation changes by two particles (between red and blue) when tuning the cavity below the Fermi level, as illustrated by the crossing of red, green, and blue dashed lines in a single point. When the matrix element Ω is finite (solid lines), the ground state of the two-particle Fock sector is, to leading order in Ω, lowered by $8\Omega^2/U$, while the odd sectors are lowered by $2\Omega^2/U$, leading to a splitting of $12\Omega^2/U$ of the two cavity levels. As a result, a $N=2$ dot-cavity ground-state singlet is formed at intermediate values $|\epsilon_{\rm c}| \lesssim 0.05\,U$ (lowest-energy green solid line) (see Appendix A for more details).

parameter range, both the dot and the cavity can be occupied by a single electron each which will combine to form a singlet.

Figure 7 shows several ground-state maps where both dot and cavity levels are tuned through the Fermi energy $\epsilon_{\rm F}$. In Fig. 7(a), we plot the dot-cavity ground-state map derived from ED as a function of applied voltages $\epsilon_{\rm d}'/U$ and $\epsilon_{\rm c}'/U$ [we include capacitive cross talk to allow for better comparison with the experimental result in Fig. 7(c), see Eqs. (14) and (15)]. We label the different ground states by $(N_{\rm d},N_{\rm c})$, where $N_{\rm d} = \sum_{\sigma} n_{\rm d}^{\sigma}$ ($N_{\rm c} = \sum_{j,\sigma} m_j^{\sigma}$) denote the total dot (cavity) occupation. The boundaries between different regions mark those configurations where the particle number on the dot-cavity system is undefined and the system conducts. For vanishingly small coupling $\Omega/U \to 0$ (dashed lines), the occupation of the cavity and the dot are independent and the dot is empty for $\epsilon_{\rm d} > 0$, singly occupied for $\epsilon_{\rm d} < 0 < \epsilon_{\rm d}+U$, and doubly occupied for $\epsilon_{\rm d} < -U$. Similarly, the cavity occupation changes by two electrons whenever a cavity level crosses the Fermi energy because charging effects on the cavity are absent. At finite dot-cavity coupling Ω (solid lines), the dot and cavity states hybridize and form an intermediate singlet ground state (see also Fig. 6). This results in a pronounced modification of the ground-state map with additional regions of odd cavity-occupation states separating regions with odd-dot–even-cavity regions. The emerging dot-cavity singlet extends over the entire hybrid system and thus defines an artificial asymmetric dot-cavity molecule (note that these molecular states are less

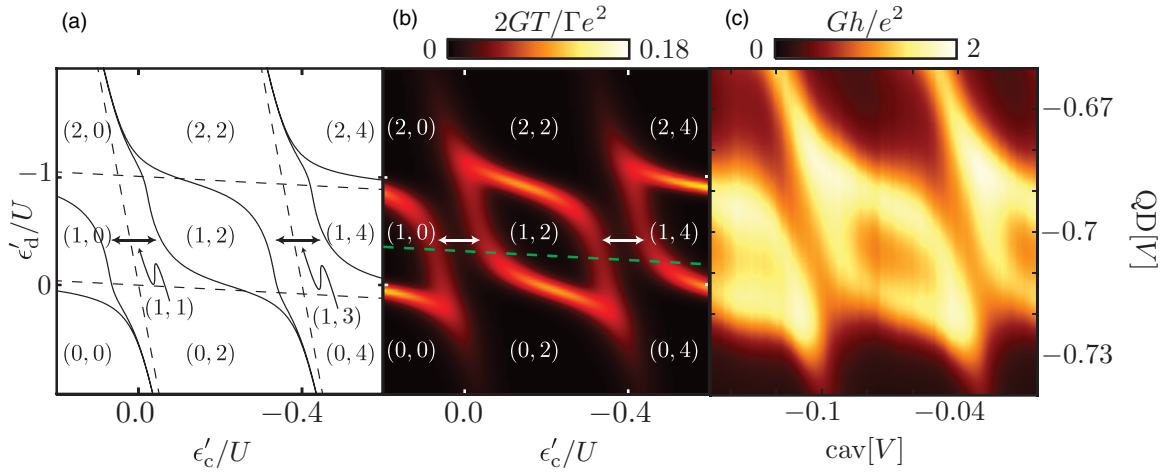

FIG. 7. Ground-state maps for a coupled dot-cavity system showing hybridization (a) from exact diagonalization (see Sec. IV), (b) from a master-equation transport analysis (see Sec. V), and (c) from transport experiments (see Ref. [23]) [theoretical results in (a) and (b) assume a capacitive cross talk between the dot and cavity, see Eqs. (14) and (15)]. Note the different scales measuring ϵ'_d/U and ϵ'_c/U, as the cavity levels are more dense than the dot's Coulomb resonances. (a) Ground-state map versus dot and cavity energies as obtained from ED. Lines indicate parameter settings where different particle occupations become degenerate, thus allowing for transport across the artificial molecule. Regimes with unique occupation are labeled with their dot, cavity occupation $(N_{\rm dot}, N_{\rm cav})$. Dashed lines refer to the decoupled case with $\Omega/U = 0$ and full lines correspond to $\Omega/U = 0.12$. A finite dot-cavity coupling Ω leads to a gap opening indicated by black arrows (of minimal width $12\,\Omega^2/U$) at $\epsilon'_d/U = -0.5$; the gap opens up a region of odd cavity occupation with a molecular-singlet formation. (b) Differential conductance $G = dI/dV$ versus dot and cavity energies for the same parameters as in (a) and rates $\Gamma_L = \Gamma_R = 5\Gamma_c \equiv \Gamma/2$. Gap openings are indicated by white arrows. The intensities of the conductance peaks depend on the tunneling rates (20) and (21), while the temperature $T/U = 0.02$ determines their broadening. Kondo physics generates an enhanced conductance when the occupation of the artificial molecule is odd, i.e., inside the $(1,2n)$ regions with n integer; such signatures are not captured by our master-equation description but show up in the experiment. In Sec. VI, we take a cut along the green dashed line and address Kondo physics. Note that in (a) and (b), we truncate the Hilbert space at three spin-degenerate cavity levels. (c) Measured differential conductance through the experimental dot-cavity device as a function of bias on the dot plunger gate and cavity gate (see Ref. [23]). The line shapes match the full black lines in (a) and the transport resonances in (b), thus confirming that the dot and cavity hybridize to form a coherent "molecule." The difference in intensities between occupancies $(1,2n)$ and $(0,2n)$, $(2,2n)$ is due to transport through a Kondo resonance.

prominent at even dot fillings). Given the large spatial extent of the cavity, the existence of such a coherent state defines a lower bound on the spin coherence length in GaAs heterostructures. It is this dot-cavity molecular singlet that competes with the dot-lead Kondo singlet and that is one of the most fascinating features characteristic of this device.

Next, we turn to the transport physics that renders the ground-state map visible in an experiment. Indeed, since linear transport is restricted to the degeneracy points where two ground states with different particle number cross, we expect that a conductivity map $G = dI/dV$ will accurately trace the lines of Fig. 7(a). In the following, we use a master-equation approach in a first attempt to map out the ground-state diagram that can be compared to experimental data [see Figs. 7(b) and 7(c), respectively]. Furthermore, such an approach can be expanded to analyze nonlinear transport at large bias $\mu_L \neq 0$. The inclusion of Kondo physics requires a more sophisticated technique and we will discuss this topic with the help of an equation-of-motion analysis in Sec. VI.

V. MASTER-EQUATION APPROACH

The master equation successfully describes the transport through interacting systems that are weakly coupled to leads [36–40], i.e., when $\Gamma_a, \Gamma_c \ll \max\{k_B T, eV\}$, where $eV = \mu_L - \mu_R$ is the bias voltage between the left and right leads, T is the temperature, and k_B is the Boltzmann constant which we set to unity $k_B = 1$. The current I across the artificial molecule is determined by the tunneling rates W between the leads and the artificial molecule, as well as its occupation probability P and the Fermi functions n_F of the leads. Here, we describe transport through the dot-cavity system as sequential, i.e., to lowest order in its couplings Γ_a and Γ_c to the leads, but treat the dot-cavity coupling Ω to all orders by using our ED results for the molecular states. Thus, in a picture where the coupling between the dot and the cavity is treated perturbatively, our analysis captures the cotunneling processes involving the dot and the cavity, which we call cavity-assisted cotunneling processes.

Given the molecular eigenstates $|\psi^\alpha_{\mathbf{N}}\rangle$ with $\mathbf{N} = (N^\uparrow, N^\downarrow)_\sigma$, we define the associated occupation probabilities $P^\alpha_{\mathbf{N}}$. Here, we distinguish the spin-tuple $(N^\uparrow, N^\downarrow)_\sigma$ describing the molecular spin occupation from the dot-cavity occupation-tuple (N_d, N_c). The occupation dynamics $\dot{P}$ is determined by the master equation

$$\partial_t P^\alpha_{\mathbf{N}} = \sum_{\mathbf{N}',\alpha'} \left(W^{\alpha,\alpha'}_{\mathbf{N},\mathbf{N}'} P^{\alpha'}_{\mathbf{N}'} - W^{\alpha',\alpha}_{\mathbf{N}',\mathbf{N}} P^\alpha_{\mathbf{N}} \right), \tag{18}$$

where the rates $W^{\alpha,\alpha'}_{\mathbf{N},\mathbf{N}'}$ describe the transitions from state $|\psi^{\alpha'}_{\mathbf{N}'}\rangle$ to state $|\psi^\alpha_{\mathbf{N}}\rangle$. Restricting the analysis to sequential tunneling processes and considering only transitions between

states that differ by one electron, the rates $W^{\alpha,\alpha'}_{\mathbf{N}\pm\mathbf{e}_\sigma,\mathbf{N}}$ take us between charge sectors $\mathbf{N}$ and $\mathbf{N}\pm\mathbf{e}_\sigma$ with $\mathbf{e}_\uparrow=(1,0)_\sigma$ and $\mathbf{e}_\downarrow=(0,1)_\sigma$. We couple the artificial molecule to the leads via the tunneling Hamiltonian $\bar{H}_{\rm tun}$ [see Eq. (11)], with the latter contributing three processes that induce changes in the occupation number of the artificial molecule. These have corresponding rates $W^{\rm L}$, $W^{\rm R}$, $W^{\rm c}$ adding up to the total transition rate

$$W^{\alpha,\alpha'}_{\mathbf{N}\pm\mathbf{e}_\sigma,\mathbf{N}}=W^{{\rm L}\,\alpha,\alpha'}_{\mathbf{N},\pm\mathbf{e}_\sigma,\mathbf{N}}+W^{{\rm R}\,\alpha,\alpha'}_{\mathbf{N}\pm\mathbf{e}_\sigma,\mathbf{N}}+W^{{\rm c}\,\alpha,\alpha'}_{\mathbf{N}\pm\mathbf{e}_\sigma,\mathbf{N}}. \tag{19}$$

Note that we sum the rates $W^{\rm R}$ and $W^{\rm c}$ incoherently (see our discussion of Fano resonances in Sec. III and Fig. 4). The individual rates are derived in Appendix B and the result is

$$W^{{\rm a}\,\alpha,\alpha'}_{\mathbf{N}\pm\mathbf{e}_\sigma,\mathbf{N}}=\frac{\Gamma_{\rm a}}{\hbar}\left|\left\langle\psi^{\alpha}_{\mathbf{N}\pm\mathbf{e}_\sigma}\middle|d^{\pm}_\sigma\middle|\psi^{\alpha'}_{\mathbf{N}}\right\rangle\right|^2 g^{\rm a}_{\pm}\left(\epsilon_{\mathbf{N}\pm\mathbf{e}_\sigma}-\epsilon_{\mathbf{N}}\right), \tag{20}$$

$$W^{{\rm c}\,\alpha,\alpha'}_{\mathbf{N}\pm\mathbf{e}_\sigma,\mathbf{N}}=\frac{\Gamma_{\rm c}}{\hbar}\left|\left\langle\psi^{\alpha}_{\mathbf{N}\pm\mathbf{e}_\sigma}\middle|f^{\pm}_\sigma\middle|\psi^{\alpha'}_{\mathbf{N}}\right\rangle\right|^2 g^{\rm R}_{\pm}\left(\epsilon_{\mathbf{N}\pm\mathbf{e}_\sigma}-\epsilon_{\mathbf{N}}\right), \tag{21}$$

where we have introduced the operator $f_\sigma=\sum_j f_{j\sigma}$. The rates $\Gamma_{\rm a}$ and $\Gamma_{\rm c}$ are given in Eqs. (12) and (13), $g^{\rm a}_+(\epsilon)=n_{\rm F}(\epsilon-\mu_{\rm a})$ and $g^{\rm a}_-(\epsilon)=1-n_{\rm F}(-\epsilon-\mu_{\rm a})$ derive from the Fermi-Dirac distribution $n_{\rm F}(\epsilon)=1/(1+e^{\beta\epsilon})$, and $\beta=1/T$. We use the operator notation $\mathcal{O}^+=\mathcal{O}^\dagger$ and $\mathcal{O}^-=\mathcal{O}$. To evaluate the rates (20) and (21), we use the eigenstates and eigenenergies from our ED analysis (Sec. IV).

The master equations (18) can be written in matrix form [38,39]

$$\partial_t\mathbf{P}=\mathbf{W}\mathbf{P}, \tag{22}$$

with an occupation probability vector $\mathbf{P}$ and the rate matrix $\mathbf{W}$ that couples the different states. For the steady state, $\mathbf{W}\mathbf{P}=0$, and we impose the normalization $\mathbf{P}\cdot\mathbf{e}=1$, where $\mathbf{e}=(1,1,\ldots)$. Defining the square matrix $\mathbf{E}$ with all its rows given by $\mathbf{e}$, we rewrite $\mathbf{W}\mathbf{P}+\mathbf{e}=\mathbf{e}$ in the form $\mathbf{W}\mathbf{P}+\mathbf{E}\mathbf{P}=\mathbf{e}$ and find that $\mathbf{P}$ can be written in the form

$$\mathbf{P}=(\mathbf{W}+\mathbf{E})^{-1}\mathbf{e}. \tag{23}$$

Once the probability vector $\mathbf{P}$ has been determined from Eq. (23), we obtain the current I through the artificial molecule from currents flowing between the dot (d) and the left lead (L):

$$I=e\sum_{\substack{\alpha,\alpha'\\ \mathbf{N},\sigma}}\left(W^{{\rm dL}\,\alpha,\alpha'}_{\mathbf{N}+\mathbf{e}_\sigma,\mathbf{N}}-W^{{\rm dL}\,\alpha,\alpha'}_{\mathbf{N}-\mathbf{e}_\sigma,\mathbf{N}}\right)P^{\alpha'}_{\mathbf{N}}, \tag{24}$$

where the first and second terms correspond to electrons entering and leaving the dot, respectively. In the following, we will calculate and analyze the differential conductance $G=dI/dV$, with $eV=\mu_{\rm L}$ the applied voltage, in units of $\Gamma e^2/T$. Note that the factor of T appears when differentiating the Fermi-Dirac distribution in the rates W with respect to the bias.

A. Equilibrium linear transport

We first analyze the equilibrium transport at low temperatures T and small bias $eV=\mu_{\rm L}$ such that $\max\{k_{\rm B}T,eV\}$ remains small compared to the level spacing within each molecular Fock sector. Under these conditions, transport involves only the ground-state configuration $\alpha=1$ in each Fock sector $(N^\uparrow,N^\downarrow)_\sigma$. For our spin-symmetric Hamiltonian, the ground-state configurations are restricted to $\mathbf{N}=(n,n)_\sigma$ and $\mathbf{N}=(n\pm1,n)_\sigma$. We limit ourselves to states with up to eight particles for computational reasons and thus $n\leqslant 4$. Calculating the linear-response current, we can plot the conductance $G_0=\lim_{V\to0}dI/dV$ as a function of the system parameters [see Fig. 7(b)]. Linear-response transport arises at the boundaries of the ground-state map where two dot-cavity molecular ground states are degenerate; in the following, we refer to these degeneracies as *molecular* resonances. While usual dot transport would show Coulomb resonances at energies $\epsilon_{\rm d}\approx0$ and $\epsilon_{\rm d}+U\approx0$, the molecular resonances give rise to additional split resonances within the Coulomb blockade regime $[\epsilon_{\rm d},\epsilon_{\rm d}+U]$ whenever a cavity level crosses the Fermi level, i.e., $\epsilon^{(j)}_{\rm c}\approx0$. The shape of these transport resonances is dictated by the formation of the molecular states and generates the conductivity map of Fig. 7(b) that is aligned with the ground-state map of Fig. 7(a). The intensities of the resonances encode the overlap between eigenstates that determine the transition rates W in Eqs. (20) and (21), while the temperature leads to their broadening. The same signatures have been observed in the experiment [23] [see Fig. 7(c)], that we take as evidence for the formation of an extended dot-cavity molecular state (the experimental data shown here are an unpublished result from the same device as in Ref. [23]).

B. Nonequilibrium linear transport

The above equilibrium analysis has provided us with some insights into the ground-state resonance structure of the dot-cavity hybrid. Going beyond this equilibrium analysis, we now investigate the system when it is driven strongly out of equilibrium. We apply a large bias $\mu_{\rm L}=eV$ to the left lead and tune the dot $\epsilon'_{\rm d}$ and cavity $\epsilon'_{\rm c}$ gates. Below, we describe how the cavity modifies the out-of-equilibrium transport signatures. We start with the dot's Coulomb diamond in the usual dot bias $\epsilon'_{\rm d}$ versus source bias $\mu_{\rm L}$ plot. The presence of the cavity then manifests itself through additional resonances within the Coulomb diamond, similar to the inelastic cotunneling features seen in a dot when including excited states [41–43]. Next, we take a cut through the diamond at fixed $\epsilon_{\rm d}$ and tune the cavity bias $\epsilon'_{\rm c}$; the molecular-singlet formation shows up most prominently in such a plot.

At finite bias eV, excited states are populated and contribute to the transport across the device. When calculating the rates in (20) and (21), all eigenstates and eigenenergies obtained by the exact diagonalization have to be included. In doing so, we account for all spin configurations $\mathbf{N}=(n,m)_\sigma$ with n and m bounded by the total number of single-particle levels in the system. We first investigate the effect of the electronic cavity on the standard Coulomb diamond by calculating the differential conductance $G=dI/dV$ and plotting the result versus dot gate voltage $\epsilon'_{\rm d}$ and source-drain bias $\mu_{\rm L}=eV$, while keeping the cavity level $\epsilon_{\rm c}$ fixed (see Fig. 8).

In the absence of the cavity, transport signatures appear when the dot levels align with the chemical potential in either lead $\epsilon_{\rm d}$ or $\epsilon_{\rm d}+U=\mu_{\rm L}$ or $\mu_{\rm R}$. Including a cavity with levels at $\epsilon^{(j)}_{\rm c}$, we expect signatures to appear when the molecular (rather than the dot) levels align with either $\mu_{\rm L}$ or $\mu_{\rm R}$. When aligning the molecular level with the right lead, the only available tuning parameter is the dot level; correspondingly,

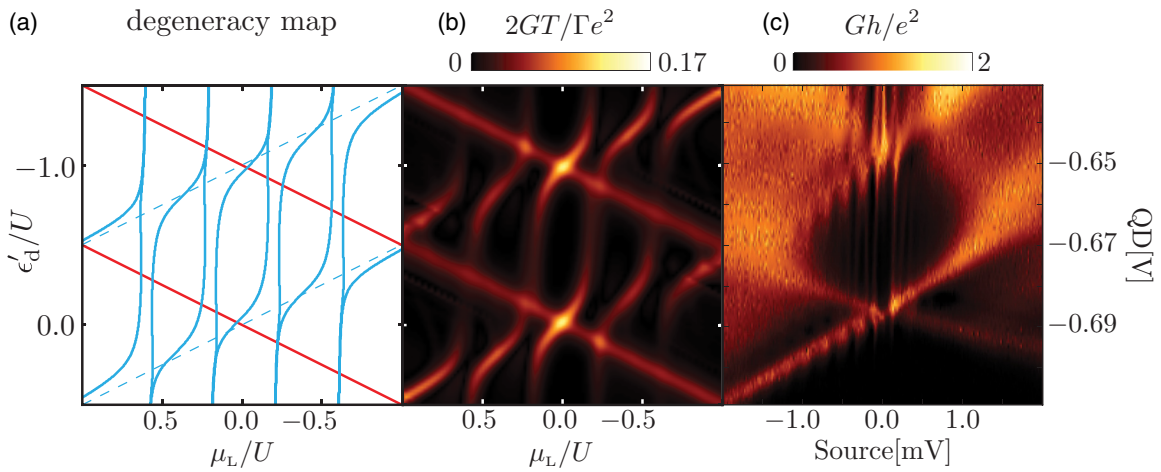

FIG. 8. Effect of the cavity on the dot Coulomb diamond. (a) Ground-state degeneracy maps for a fixed cavity level ϵ_c as a function of dot gate voltage ϵ_d' and chemical potential $\mu_L = eV$ of the left lead; shown are the calculated locations of ground-state degeneracies in the addition spectra for the dot-cavity system with four cavity levels ($\epsilon_c - \epsilon_F = -0.6U$ and $\delta_c = 0.4U$) when the artificial dot-cavity molecule is coupled to the left lead (blue) and the right lead (red). The dashed lines are for vanishing dot-cavity coupling $\Omega = 0$ while the solid lines refer to a finite $\Omega = 0.08U$. These degeneracy lines provide an outline for the out-of-equilibrium transport signatures in (b). The blue lines are susceptible to both dot and cavity parameters $\epsilon_d - \mu_L$ and $\epsilon_c - \mu_L$ that are changed by the variation of ϵ_d' and μ_L. The red lines, instead, depend on the parameters $\epsilon_d - \mu_R$ and $\epsilon_c - \mu_R$. The latter is independent of ϵ_d' and μ_L and, hence, the red lines do not show any features related to the cavity. (b) Transport resonances as a function of dot gate voltage ϵ_d' and chemical potential $\mu_L = eV$ as derived from a master-equation approach assuming a capacitive cross talk between the dot gate and the chemical potential of the left lead as explained in Sec. III [Eqs. (14) and (15)]. The same dot-cavity system as in (a) is now simultaneously coupled to both leads at temperature $T = 0.02U$ with rates $\Gamma_L = \Gamma_R = 5\Gamma_c = \Gamma/2$. The transport resonances trace the degeneracies shown in (a): positively sloped Coulomb resonances (where the chemical potential $\mu_L = eV$ is aligned with the dot) are strongly modified by the cavity states, while the negatively sloped resonances remain largely unperturbed, as expected from the schematic view offered by the two spectra in (a). While the small splitting due to the molecular singlet formation shows up in the spectral map (a), this feature is not visible in the transport map shown in (b) due to the temperature broadening; it will show up in Fig. 9(c) at large coupling Ω. The vertical features showing up when the dot is in Coulomb blockade appear in a location where one expects cotunneling features to manifest. In fact, our molecular description via ED captures processes which correspond to two-particle cotunneling processes in a perturbative dot-cavity treatment (see Fig. 9 for details). (c) Measured differential conductance through the dot-cavity device as a function of dot bias (vertical axis) and source-drain bias across the device (horizontal axis) (see Ref. [23]). The cavity levels generate avoided crossings on the positively slanted Coulomb resonances as predicted by our theoretical analysis, emphasizing the formation of a molecular singlet state. In the experiment, the cavity levels are more densely spaced as compared to our theoretical modeling, where we have limited ourselves to four cavity levels due to computational reasons.

we take a near vertical cut at fixed cavity energy ϵ_c through the molecular ground-state map in Fig. 7, leaving its qualitative behavior unchanged. On the other hand, the left lead can be aligned with the molecular level via two parameters: the dot level ϵ_d and the chemical potential μ_L in the left lead (which in turn changes the cavity levels $\epsilon_c^{(j)}$) and we thus expect to explore the entire ground-state map in Fig. 7. The expected transport signatures are shown in Fig. 8(a) where we plot the locations where additional molecular (ground-state) degeneracies enter/leave the bias window. At these locations, the degeneracies between molecular states and a lead chemical potential add or remove a transport channel, producing a signal in the nonlinear conductivity G.

The degeneracy map of Fig. 8(a) then has to be compared with the transport map in Fig. 8(b) where we plot the differential conductance calculated from Eq. (24). As expected, the boundaries of the Coulomb diamond are modulated by the presence of the cavity with anti-crossings appearing whenever cut by $\epsilon_c^{(j)}$. These anticrossings appear on the positively sloped Coulomb resonance when the chemical potential in the left lead lines up with the molecular degeneracies. The negatively sloped lines originate from aligning the dot level with the right chemical potential via the direct dot-lead coupling. No signatures appear due to the cavity as $\epsilon_c^{(j)}$ remains fixed with respect to μ_R; in Figs. 8(a) and 8(b), we set all cavity levels $\epsilon_c^{(j)}$ far away from the chemical potential in the right lead μ_R. As in the equilibrium situation, the intensities of the high conductance lines are given by the wave-function overlaps in Eqs. (20) and (21), while their broadening is due to the temperature $k_B T = 0.02U$. Figure 8(c) shows the corresponding out-of-equilibrium transport data measured in the dot-cavity device of Ref. [23]. We observe a good qualitative agreement with our model predictions, noting that we have assumed a lower density of cavity levels in our theoretical analysis due to computational reasons.

The appearance of additional resonances within the Coulomb diamonds is well known from conventional dots: accounting for the dot's excited states, higher-order transport channels open up (or close) when multiparticle processes become allowed (or disallowed), thereby changing the total current through the dot; such changes then generate (weaker) resonance structures in the differential conductance G and are known as inelastic cotunneling features. We can cast the appearance of our molecular resonance structure due to the

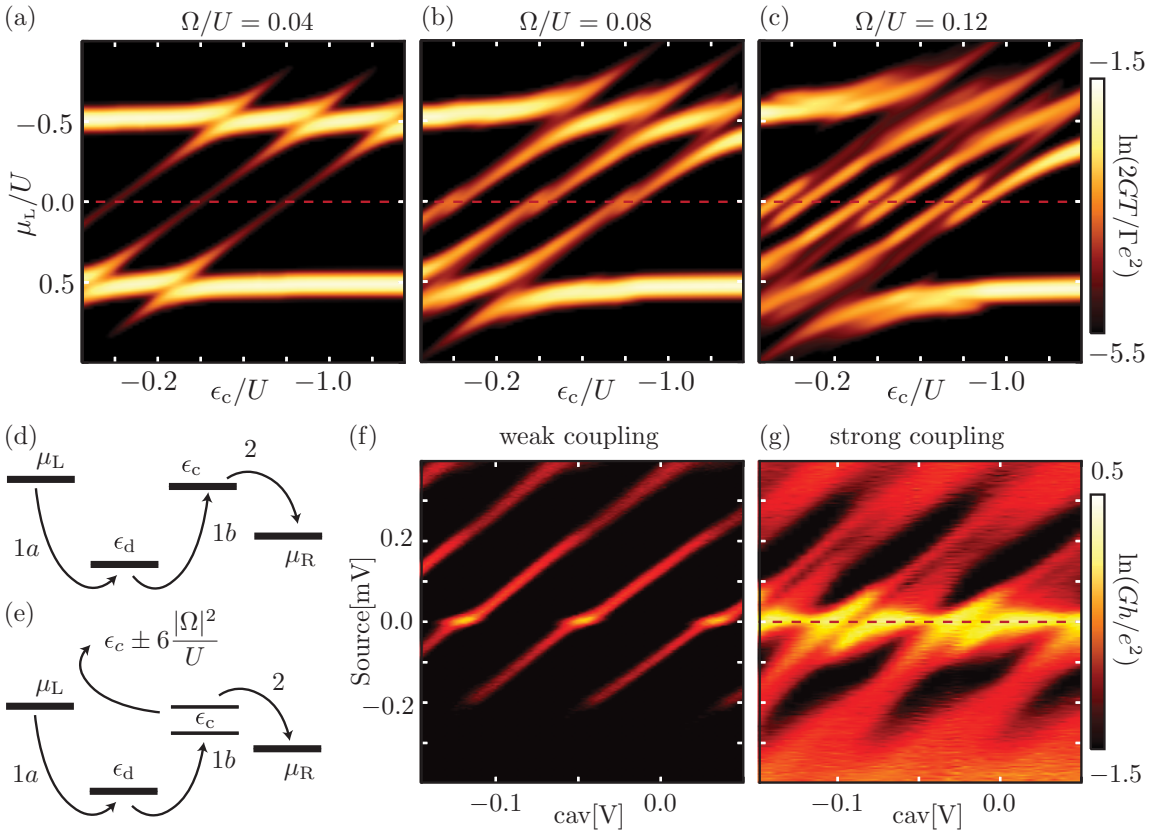

FIG. 9. Differential conductance in the Coulomb blockade region at fixed dot level ϵ_d versus source bias μ_L and cavity level ϵ_c for different dot-cavity couplings Ω. A logarithmic scale is used in order to highlight the weak cotunneling features. The dot is placed at the particle-hole symmetric point within the blockaded region $\epsilon_d = -U/2$, the temperature is set to $T = 0.02\,U$, and the leads are coupled to the artificial molecule through the rates $\Gamma_L = \Gamma_R = 5\Gamma_c = \Gamma/2$. The two horizontal lines mark the dot's Coulomb peaks and the array of weak diagonal lines is due to the molecular resonances (or cavity-assisted cotunneling processes) appearing as the next cavity level $\epsilon_c^{(j)}$ is shifted across μ_R. These resonances are suppressed due to the indirect coupling of the cavity (via the dot) to the left lead and it is the hybridization with the dot that leads to the transport signature. Increasing the coupling Ω, the cavity degeneracy is first slightly lifted [see (b)] and then fully lifted with a splitting $\sim 12\,\Omega^2/U$ in (c); (a)–(c) include three spin-degenerate cavity levels. The red dotted line marks the location where Kondo transport would be present (not captured by the master-equation analysis discussed in this section). (d) Illustration of a cavity-assisted cotunneling process: the arrows represent hopping events with $1a$ and $1b$ describing a two-electron cotunneling event from the left lead into the cavity via the dot. The arrow labeled by 2 marks a single-electron tunneling from the cavity into the right lead. (e) The same process including the splitting of the cavity level due to the hybridization with the dot, corresponding to the split cotunneling signatures in (b) and (c). (f), (g) Differential conductance measurements through the dot-cavity device [23]. (f) Weak coupling $\Omega \ll t_L$ and (g) strong coupling $\Omega \gg t_L$. Although the splitting is accurately captured in the master-equation approach [see (c)], the additional Kondo resonance along the zero source-drain bias line (source = 0) is not captured by the result of the master-equation approach in (c).

presence of the cavity in this language as well; rather than a complex dot spectrum, it is the dot-cavity hybridization that generates these features. Formulating the transport within a perturbative picture in the dot-cavity coupling Ω, the additional resonances then are viewed as cavity-assisted cotunneling processes involving two-electron processes, i.e., a coherent hopping of one electron from the left lead to the dot, while the (second) dot electron moves out of the way by hopping to the cavity (see Fig. 9). Note that, in making use of exact molecular states, our description includes processes to lowest order in the coupling to the leads and all orders in the coupling Ω between the dot and the cavity and thus goes beyond the cotunneling result.

Next, we focus on the transport signatures at a fixed dot level ϵ_d when tuning the source (μ_L) and cavity level ϵ_c (see Fig. 9). We place the dot level into the blockaded position $\epsilon_d \approx -U/2$ at zero bias $\mu_L = 0$ with one electron on the dot. Figure 9 then shows the Coulomb blockaded region between two subsequent Coulomb peaks. As the dot couples to the right lead directly via t_R, the dotlike molecular resonances appear as bright horizontal features whenever a dot level is aligned with the left lead at finite bias μ_L. The weak (diagonal) features are associated with the cavitylike molecular levels and appear whenever a cavity level enters/leaves the bias window between μ_L and μ_R. These molecular resonances involve little, $\propto\Omega^2$, spectral weight on the dot and hence are largely suppressed [see the weak transport features in Fig. 9(a)]. Increasing the coupling Ω, the singlet gap $12\Omega^2/U$ in the molecular spectrum and the spectral weight on the dot increase; this manifests itself in the transport as an increased intensity and splitting of the molecular features [see Figs. 9(b) and 9(c)]. All transport signatures, except for the Kondo resonance at zero source bias, compare well with the experimental findings shown in

Figs. 9(f) and 9(g). The observed splitting of the cavity level confirms that the transport across the device involves the spin-coherent dot-cavity singlet.

In the above discussion, we have treated the dot-cavity system as a single artificial molecule and have analyzed the transport as sequential tunneling from the left lead via the artificial molecule to the right lead. Alternatively, we can formulate the transport via the dot-cavity system as a cotunneling process involving two electrons and the dot and cavity as two separate entities. The jump from the left lead to the cavity (and subsequently to the right lead) then involves the dot in a virtual process which contributes a factor $\propto\Omega^2$ [see Fig. 9(d)]. This process is turned on/off as the cavity level enters/leaves the bias window. In Fig. 9(e), we show the same process at large coupling, where the cavity level is split by the presence of the dot, resulting in two closeby cotunneling features separated by the singlet gap $12\Omega^2/U$. We call this process a cavity-assisted cotunneling process, where the virtual hop through the dot is helped by the presence of the cavity by providing a large final density of states. Note that (i) in Ref. [41], we have shown that such cavity-assisted cotunneling processes provide further spectroscopic information on the dot. (ii) Within the cotunneling picture, we have to artificially account for the cavity-level splitting. On the contrary, the discussion based on the molecular picture relies on the exact solution of the dot-cavity problem; this includes all orders of tunneling (Ω) between the dot and the cavity and thus provides us with the proper level splitting.

The experimental data in Fig. 9(g) exhibit an additional zero-bias peak due to the Kondo effect. This Kondo resonance is due to a singlet formation between the dot and the leads and is broken up by the dot-cavity molecular singlet when the cavity is tuned across the equilibrium chemical potential. The switching between a many-body Kondo- and a dot-cavity molecular singlet is one of the outstanding results of Ref. [23]; its theoretical understanding will be developed in the next section.

VI. EQUATION OF MOTION

To analyze the competition between Kondo physics and dot-cavity hybridization, we make use of an equation-of-motion (EOM) technique [33] and focus on the equilibrium linear-response properties. The EOM method is ubiquitous in the discussion of quantum-dot physics described by the Anderson impurity model [44–49]; it provides us with the dot Green's function $G_\sigma(\omega)$, from which we obtain the conductance G_0 of the device through a modified Meir-Wingreen formula [50] as discussed in Appendix C for the limit of finite but small temperatures $T \ll \Gamma$. In this limit, we recover the standard expression [49,50]

$$G_0 = -\frac{e^2}{h}\tilde{\Gamma}(\epsilon_{\rm F})\sum_\sigma 2\,\mathrm{Im}\,G_\sigma(\epsilon_{\rm F}), \tag{25}$$

with the rate $\tilde{\Gamma}$ derived in Appendix C:

$$\tilde{\Gamma}(\epsilon_{\rm F}) = \frac{\Gamma}{2}\frac{1+\beta}{2+\beta}, \quad \beta = 2\frac{\Gamma_{\rm c}}{\Gamma}\frac{\Omega^2}{\epsilon_{\rm c}^2+\Gamma_{\rm c}^2/4}. \tag{26}$$

Here, we have considered a minimal situation with a single-cavity level and $\Gamma_{\rm R} = \Gamma_{\rm L} = \Gamma/2$; the rate (26) is then bounded by $\Gamma/4 < \tilde{\Gamma} < \Gamma/2$. Aligning the cavity with the Fermi level, we have $\epsilon_{\rm c} = 0$ and tuning Ω from weak to strong coupling, the parameter β changes from a small value to one above unity. The strong coupling is exemplified in Fig. 9(g), where the competition between Kondo and molecular singlets is prominent.

The following discussion makes use of Hamiltonian (3) in the compact notation:

$$H = \sum_\sigma \epsilon_{\rm d} d_\sigma^\dagger d_\sigma + U n_\uparrow n_\downarrow + \sum_{k,\sigma}\epsilon_k c_{k\sigma}^\dagger c_{k\sigma} + \sum_{k,\sigma}(t_k d_\sigma^\dagger c_{k\sigma} + \text{H.c.}), \tag{27}$$

where t_k encodes all tunnelings to and from the dot; Fano-type interference effects have to be excluded as discussed in Sec. III. In Appendix E, we show that within our EOM analysis, the Hamiltonian (27) is equivalent to $\bar{H}$ [see Eq. (8) and Fig. 3(b)]. When using the Hamiltonian (27), the couplings $t_{\rm L}$, Ω, and $t_{\rm R}$ are accounted for in the same order.

A. Formalism and lowest-order approximation

For completeness, we provide a brief overview of the equation-of-motion method leading to the dot Green's function G_σ and highlight the physical implications of the different truncation schemes (see Refs. [46–49] and Appendix D for more details). We start with the retarded thermal Green's functions of the dot

$$G_\sigma = -i\lim_{\eta\to 0^+}\int_{-\infty}^{\infty} dt\,\Theta(t)\langle\{d_\sigma(t), d_\sigma^\dagger(0)\}\rangle e^{i(\omega+i\eta)t}, \tag{28}$$

where $\langle\ldots\rangle$ denotes the finite-temperature quantum-statistical average and Θ is the Heaviside function. The equation of motion for the (retarded) Green's function G_σ generates an infinite hierarchy of additional equations for higher-order Green's functions including lead electrons. It is convenient to introduce the Zubarev notation [51] (with A and B two fermionic operators)

$$\langle\langle A; B\rangle\rangle_z = \mp i\lim_{\eta\to 0^+}\int_{-\infty}^{\infty} dt\,\Theta(\pm t)\langle\{A(t), B(0)\}\rangle e^{i(\omega\pm i\eta)t}, \tag{29}$$

with the shorthand $z = \omega \pm i\eta$ for the complex frequency; we will suppress this subscript from now on. The EOMs for such Green's functions are found by taking time derivatives and transforming to frequency space,

$$\begin{aligned} z\langle\langle A; B\rangle\rangle &= \langle\{A, B\}\rangle + \langle\langle [A, H]; B\rangle\rangle \\ &= \langle\{A, B\}\rangle - \langle\langle A; [B, H]\rangle\rangle, \end{aligned} \tag{30}$$

where $(\{\cdot,\cdot\})$ $[\cdot,\cdot]$ denote usual (anti)commutators. Applying these equations to the dot Green's function and the dot-lead correlator $\langle\langle c_{k\sigma}; d_\sigma^\dagger\rangle\rangle$, and eliminating the latter, we obtain [33] ($\bar{\sigma}$ and σ denote complementary spins)

$$G_\sigma(z) \equiv \langle\langle d_\sigma; d_\sigma^\dagger\rangle\rangle = \frac{1 + U\langle\langle n_{\bar{\sigma}} d_\sigma; d_\sigma^\dagger\rangle\rangle}{z - \epsilon_{\rm d} - \Sigma(z)}, \tag{31}$$

where the dot-lead correlator gives rise to the network self-energy (see Appendix E)

$$\Sigma(\omega \pm i\eta) = \mp i\frac{\Gamma_{\rm L}+\Gamma_{\rm R}}{2} + \frac{|\Omega|^2}{\omega - \epsilon_{\rm c} \pm i\Gamma_c/2}. \tag{32}$$

The noninteracting limit $U = 0$ of Eq. (31) provides us with a Lorentzian spectrum centered around the (spin-degenerate) dot level $\epsilon_{\rm d}$. At finite U, we first truncate at the level of the four-point Green's function in (31); using a cumulant expansion, we obtain

$$\langle\langle n_{\bar\sigma} d_\sigma; d_\sigma^\dagger\rangle\rangle \approx \langle n_{\bar\sigma}\rangle\langle\langle d_\sigma; d_\sigma^\dagger\rangle\rangle \tag{33}$$

(see Refs. [47–49,52] and Appendix D for details). This truncation is $O(t^0)$ and provides a shift $U\langle n_{\bar\sigma}\rangle$ in the dot level depending on its filling. We must therefore replace $\epsilon_{\rm d} \to \epsilon_{\rm d} + U\langle n_{\bar\sigma}\rangle$ in the $U = 0$ Green's function. To calculate the occupation on the dot, we can use the spectral theorem

$$\langle n_{\bar\sigma}\rangle = \frac{i}{2\pi}\oint dz\, n_{\rm F}(z) G_\sigma(z), \tag{34}$$

where the integration contour runs clockwise around the real axis with the advanced Green's function ($G_\sigma^{\rm a} = G_\sigma^*$) in the lower half of the complex plane. As we work at equilibrium with $V = 0$, the same Fermi-Dirac distribution $n_{\rm F}(\omega)$ applies to all the leads. Combining the results for G_σ and $\langle n_{\bar\sigma}\rangle$ self-consistently, the conductance $G_0(\epsilon_{\rm d})$ then exhibits Lorentzian peaks [33] around $\epsilon_{\rm d} = 0$ and $-U$.

B. Lacroix and further truncation schemes

Proceeding with the next order, the equation of motion for the four-point Green's function in (31) takes the form

$$\begin{aligned}(z - \epsilon_{\rm d} - U)\langle\langle n_{\bar\sigma} d_\sigma; d_\sigma^\dagger\rangle\rangle &= \langle n_{\bar\sigma}\rangle + \sum_k [t_k\langle\langle n_{\bar\sigma} c_{k\sigma}; d_\sigma^\dagger\rangle\rangle \\ &\quad + t_k\langle\langle d_{\bar\sigma}^\dagger c_{k\bar\sigma} d_\sigma; d_\sigma^\dagger\rangle\rangle - t_k^*\langle\langle c_{k\bar\sigma}^\dagger d_{\bar\sigma} d_\sigma; d_\sigma^\dagger\rangle\rangle]\end{aligned} \tag{35}$$

and introduces three new correlators involving a lead state $k\sigma$ or $k\bar\sigma$. The second term $t_k\langle\langle d_{\bar\sigma}^\dagger c_{k\bar\sigma} d_\sigma; d_\sigma^\dagger\rangle\rangle$ in the sum describes a spin exchange between the dot and a lead electron involving a tunneling process and is the basic process responsible for the Kondo resonance. Truncating the EOM at this $O(t)$ level is not sufficient to capture the Kondo effect, as the last two terms cancel (see Appendix D). Nonetheless, it is instructive to note that the corresponding dot Green's function

$$G_\sigma(z) = \frac{1 - \langle n_{\bar\sigma}\rangle}{z - \epsilon_{\rm d} - \Sigma(z)\left(1 + \frac{U\langle n_{\bar\sigma}\rangle}{z - (\epsilon_{\rm d}+U)}\right)} \tag{36}$$

$$+ \frac{\langle n_{\bar\sigma}\rangle}{z - (\epsilon_{\rm d}+U) - \Sigma(z)\left(1 - \frac{U(1-\langle n_{\bar\sigma}\rangle)}{z-\epsilon_{\rm d}}\right)} \tag{37}$$

now shows two split Lorentzians as a function of z, one centered around $\epsilon_{\rm d}$ and the other around $\epsilon_{\rm d} + U$, respectively. Proceeding with the equations of motion for the three four-point Green's functions including a lead electron and truncating at order $O(t^2)$, i.e., using the Lacroix truncation [44,45,47], one arrives at the relations

$$\sum_k t_k\langle\langle n_{\bar\sigma} c_{k\sigma}; d_\sigma^\dagger\rangle\rangle = \langle\langle n_{\bar\sigma} d_\sigma; d_\sigma^\dagger\rangle\rangle\,\Sigma(z), \tag{38}$$

$$\sum_k t_k\langle\langle d_{\bar\sigma}^\dagger c_{k\bar\sigma} d_\sigma; d_\sigma^\dagger\rangle\rangle = \langle\langle n_{\bar\sigma} d_\sigma; d_\sigma^\dagger\rangle\rangle\,\Sigma(z) + [1 + \Sigma(z)G_\sigma(z)]P_{\bar\sigma}(z) - G_\sigma(z)Q_{\bar\sigma}(z), \tag{39}$$

$$-\sum_k t_k^*\langle\langle c_{k\bar\sigma}^\dagger d_{\bar\sigma} d_\sigma; d_\sigma^\dagger\rangle\rangle = -\langle\langle n_{\bar\sigma} d_\sigma; d_\sigma^\dagger\rangle\rangle\,\Sigma(z_2) + [1 + \Sigma(z)G_\sigma(z)]P_{\bar\sigma}(z_2) + G_\sigma(z)Q_{\bar\sigma}(z_2), \tag{40}$$

with the shifted variable

$$z_2 = 2\epsilon_{\rm d} + U - z. \tag{41}$$

Equations (38)–(40) express the various dot-lead correlators in terms of the four-point dot correlator $\langle\langle n_{\bar\sigma} d_\sigma; d_\sigma^\dagger\rangle\rangle$, the dot Green's function G_σ, and self-energy Σ, as well as the two new functions [47]

$$P_\sigma(z) \equiv \sum_k \frac{t_k\langle d_\sigma^\dagger c_{k\sigma}\rangle}{z - \epsilon_k} = \mathcal{F}_{\sigma z}[G], \tag{42}$$

$$Q_\sigma(z) \equiv \sum_{kk'} \frac{t_{k'}t_k^*\langle c_{k\sigma}^\dagger c_{k'\sigma}\rangle}{z - \epsilon_k'} = \mathcal{F}_{\sigma z}[1 + \Sigma G]. \tag{43}$$

The last equalities describe the functions $P_\sigma(z)$ and $Q_\sigma(z)$ in terms of an integral over the dot Green's function G_σ (see Ref. [47] and Appendix D), e.g.,

$$\mathcal{F}_{\sigma z}[G] \equiv \frac{i}{2\pi}\oint_C dz' n_{\rm F}(z') G_\sigma(z')\frac{\Sigma(z') - \Sigma(z)}{z - z'}, \tag{44}$$

and similar for $\mathcal{F}_{\sigma z}[1 + \Sigma G]$. Note that $\langle d_\sigma^\dagger c_{k\sigma}\rangle$ and $\langle c_{k\sigma}^\dagger c_{k'\sigma}\rangle$ relate to $\langle\langle d_\sigma\ ; d_\sigma^\dagger\rangle\rangle = G_\sigma$ via the spectral theorem and the equations of motion. Combining the equations (31), (35), and (38)–(40), the final expression for the dot Green's function is [47]

$$G_\sigma(z) = \frac{g_2^{-1}(z) + \langle n_\sigma\rangle U + [P_{\bar\sigma}(z) + P_{\bar\sigma}(z_2)]U}{g_2^{-1}(z)\,g^{-1}(z) - [P_{\bar\sigma}(z) + P_{\bar\sigma}(z_2)]U\,\Sigma(z) + [Q_{\bar\sigma}(z) - Q_{\bar\sigma}(z_2)]U}, \tag{45}$$

where we have introduced the characteristic functions

$$g^{-1}(z) = [z - \epsilon_d - \Sigma(z)], \tag{46}$$

$$g_2^{-1}(z) = [z - (\epsilon_d + U) - 2\Sigma(z) + \Sigma(z_2)], \tag{47}$$

that define the poles associated with the two dot levels separated by U. The set of equations (42), (43), and (45) can be solved numerically for a self-consistent solution providing the dot's Green's function G_σ, from which the conductance at the Fermi energy follows through the Meir-Wingreen [50] formula (25).

Before discussing the result, we analyze the various features in the Green's function (45) at the positions $z = \epsilon_d, 0, 2\epsilon_d + U, \epsilon_d + U$ (see the dashed green line in Fig. 10). The functions $g^{-1}(z)$ and $g_2^{-1}(z)$ account for the Lorentzian-shaped dot levels at ϵ_d and $\epsilon_d + U$. The functions $P(z)$ and $Q(z)$ contribute additional divergences (at $T = 0$) at the Fermi level $z = \epsilon_F = 0$ and thus give rise to the Kondo unit conductance. On the other hand, at $z = 2\epsilon_d + U$ ($z_2 = 0$) it is $P(z_2)$ and $Q(z_2)$ that diverge and we obtain an unphysical negative conductance, a well-known artifact of the Lacroix truncation scheme [47]. Away from the particle-hole symmetric point, these two divergences appear in separate points ($z_2 \neq -z$) as illustrated in Fig. 10. Tuning towards the particle-hole symmetric point, the two divergences interfere and the Kondo peak vanishes.

There are several approaches that allow to cure the anomaly appearing at $z_2 = 0$, among them higher truncation schemes [48,53,54] or numerical methods [55–58]. One possibility is to replace the self-consistent determination of Q_σ in Eq. (43) by a predetermined function of Σ [53] within a generalized Lacroix scheme. A step beyond the Lacroix scheme that avoids the anomaly at $z_2 = 0$ while keeping the Kondo peak at $z = 0$ is adopting a so-called $O(t^4)$ decoupling method [48,54]; this provides expressions for the self-energies associated with the four-point functions $\langle\langle d_{\bar\sigma}^\dagger c_{k\bar\sigma} d_\sigma; d_\sigma^\dagger \rangle\rangle$ (Kondo) and $\langle\langle c_{k\bar\sigma}^\dagger d_{\bar\sigma} d_\sigma; d_\sigma^\dagger \rangle\rangle$ (anomaly). One then finds [48,49] that the self-energy for the spin-flip excitations responsible for the Kondo effect vanishes in the Coulomb blockade region; the resulting excitations are long lived and contribute to the transport. On the contrary, the excitations at $z_2 = 0$ have finite self-energies; they are short lived and do not contribute to transport. A precise numerical approach makes use of the renormalization group and has been used in various embedded impurity systems [55,56], in the Kondo-box problem [25], and most recently for the present experiment [59] using a model Hamiltonian different from ours, i.e., without removing the Fano interference term (see Fig. 4), and a sharp Kondo peak surviving at all values of cavity energies, at variance with the experimental findings and our results presented below. Here, we choose to keep the Lacroix truncation scheme and stay away from the dangerous particle-hole symmetric point. Furthermore, we invoke Fermi-liquid arguments [60] to confirm the validity of our findings.

C. Results

The above EOM method describes Kondo physics and can be applied directly to our dot-cavity-leads system as the cavity appears only within the definition of the network self-energy Σ (see Appendix E). To obtain the transport features, we must solve Eqs. (42), (43), and (45) self-consistently. This can be done numerically or, in principle, in the zero-temperature limit analytically. Here, we shortly comment on the $T = 0$ analytic approach that provides us with a useful upper bound on the conductance that turns exact in the limits $\epsilon_c \to 0, \infty$ for $\epsilon_d = -U/2$. However, this method is unsuitable in describing a situation with a nontrivial self-energy $\Sigma(\omega)$ as is the case for our dot-cavity setup. We therefore resort to a self-consistent numerical analysis and find that the results properly explain the changeover from Kondo to molecular singlet, thus providing insights beyond the master-equation method in Sec. V.

In the zero-temperature limit, following Ref. [47], we can isolate the divergent terms in the numerator and denominator

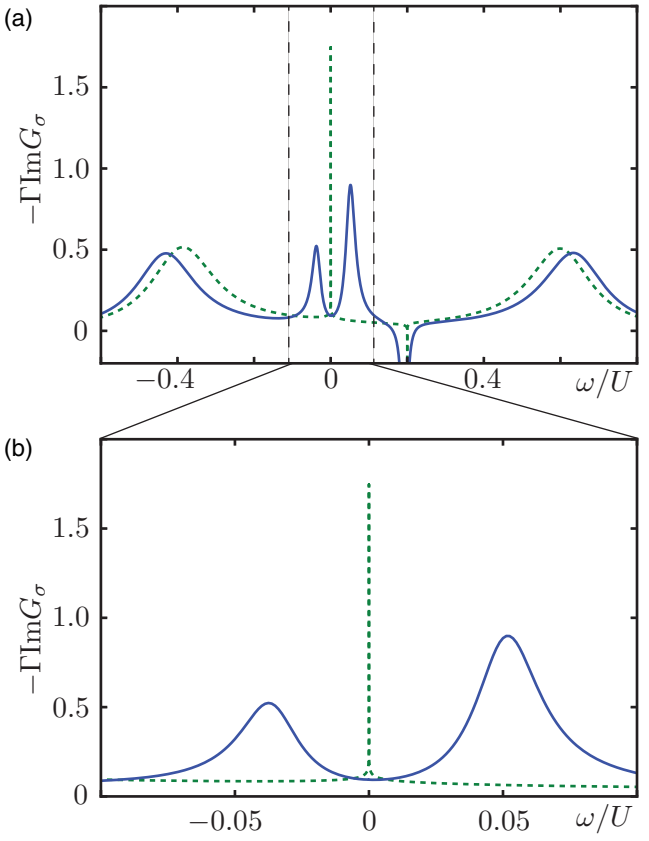

FIG. 10. Dot density of states $\mathrm{Im}G_\sigma$ obtained through the EOM method versus energy ω/U. The dashed green line shows the density of states in the dot without a cavity as a function of energy for $2\Gamma_L = 2\Gamma_R = 5\Gamma_c = \Gamma = U/10$ and in the Coulomb blockade regime with $\epsilon_d = -2U/5$ as calculated self-consistently using (45) at a temperature $T \ll T_K$. We find the expected Coulomb resonances at $\omega/U = -\frac{2}{5}, \frac{3}{5}$ in (a) and a sharp Kondo resonance at the Fermi energy $\omega = 0$ The negative peak at $\omega = 2\epsilon_d + U = U/5$ is an artifact of the Lacroix truncation. The solid blue line shows the same dot configuration with the dot coupled to a cavity with a strength $\Omega = \Gamma = 0.1U$ and the single-cavity level $\epsilon_c = 0$ tuned to the Fermi energy. Outside the region marked by the thin vertical dashed lines (a) the features remain essentially unchanged. The lower plot (b) shows an enlargement of the area around the Fermi energy. A finite coupling to the cavity suppresses the Kondo peak and establishes a pair of molecular resonances separated by $12\alpha\Omega^2/U$ [see Eq. (53)].

of G_σ close to the Fermi energy $z = \epsilon_F$ and obtain

$$G_\sigma(0) = \lim_{z\to 0} \frac{1}{Q_{\bar\sigma}(z)/P_{\bar\sigma}(z) - \Sigma(z)}. \tag{48}$$

Expanding the functional (44) around $\omega = 0$ at $T = 0$ and canceling diverging contributions, we find that

$$G_\sigma(0) = \frac{1}{1/G^*_\sigma(0) - \Sigma + \Sigma^*}, \tag{49}$$

from which follows the relation $\mathrm{Im}G_\sigma^{-1}(0) = -\mathrm{Im}\Sigma(0)$, i.e., $\mathrm{Im}G_\sigma^{-1}(0)$ is given by the network self-energy. This is the first of a set of Fermi-liquid relations [60] and is respected by the EOM in the Lacroix truncation scheme. However, using this scheme, we have no direct handle on $\mathrm{Re}G_\sigma^{-1}(0)$ at zero temperature. Commonly, one constrains the real part of the inverse Green's function using Friedel's sum rule [60]

$$\mathrm{Re}G_\sigma^{-1}(0) = [\mathrm{Im}\Sigma(0)]\cot(\pi\tilde n_\sigma), \tag{50}$$

$$\tilde n_\sigma - \langle n_\sigma\rangle \equiv \gamma = \frac{1}{\pi}\mathrm{Im}\int d\omega\, n_F(\omega)\frac{\partial\Sigma(\omega)}{\partial\omega}G_\sigma(\omega). \tag{51}$$

Equation (50) is the second of two Fermi-liquid relations and is violated in the Lacroix truncation of the EOM method.

For unstructured leads with a constant self-energy, one finds that $\gamma = 0$; furthermore, $\langle n_\sigma\rangle = \frac{1}{2}$ for a half-filled dot in Coulomb blockade and hence the real part $\mathrm{Re}G_\sigma^{-1}(0) = 0$ vanishes. As a result, the conductance of the system at zero temperature assumes its maximal value [47] $G_0 = 2e^2/\hbar$. For the structured lead, the parameter γ must be evaluated using the (self-consistent) solution for the Green's function $G_\sigma(\omega)$. Furthermore, the occupation of the dot $\langle n_\sigma\rangle$ may deviate from $\frac{1}{2}$ when the network self-energy Σ is not symmetric around the Fermi energy and must be calculated as well. However, the conductance obtained by setting $\tilde n = \frac{1}{2}$ defines an upper bound on the conductance that can be shown [61] to become a very good approximation to the exact result around $\epsilon_c = 0$. In the following, we make use of a numerical self-consistent solution of Eqs. (42)–(45) and use the Fermi-liquid relations at $\epsilon_c = 0$ to substantiate our numerical EOM results.

The functions $P_\sigma(z)$ and $Q_\sigma(z)$ in (45) depend themselves on the dot's Green's function $G_\sigma(z)$, such that we have to solve (45) via an iterative approach. In our numerical solution, we take account of one cavity mode and make use of the self-energy $\Sigma(z)$ as given by (32). We initiate the iteration with a Green's function that is peaked around the two Coulomb resonances $\epsilon_d < 0$ and $\epsilon_d + U > 0$ and proceed until convergence is achieved. The discretization of energies around $z = 0$ and $z_2 = 0$ must be sufficiently fine on the level of the Kondo temperature [62] T_K, which sets the width of the Kondo peak at $z = 0$. The green dashed line in Fig. 10 shows the standard dot-lead result (i.e., $\Omega = 0$) for the dot spectral function $-\mathrm{Im}G_\sigma(z)$ away from the dot particle-hole symmetric point, i.e., $\epsilon_d \neq -U/2$. In this regime, the Lacroix truncation works well, and the Kondo peak at $\omega = 0$ is framed by the Coulomb resonances at $\omega = \epsilon_d$ and $\epsilon_d + U$ with $\epsilon_d = -2U/5$ in Fig. 10. The width of the Coulomb resonances is set by $\Gamma/2 = U/20$ (we choose $\Gamma/2 = \Gamma_L = \Gamma_R$), while in the present approximation the width of the Kondo peak is given by the Kondo temperature [47–49]

$$T_K = (2\epsilon_d + U)\exp\left[\frac{2\pi\epsilon_d(\epsilon_d + U)}{\Gamma U}\right], \tag{52}$$

which underestimates the true width[1] (note that $\epsilon_d < 0 < \epsilon_d + U$).

The blue solid line (Fig. 10) shows the same result in the presence of a cavity (i.e., $\Omega \neq 0$) at $\epsilon_c = 0$: the Kondo peak has vanished, giving way to two molecular states separated by $12\alpha\Omega^2/U$, where the enhancement

$$\alpha = \frac{1}{1 - (1 + 2\epsilon_d/U)^2} \tag{53}$$

accounts for deviation from the dot's particle-hole symmetric point ($\epsilon_d \neq -U/2$) (see Appendix A for details).

Such a changeover from a dot-lead (Kondo) to a dot-cavity (molecular) singlet has been observed in the experiment [see Fig. 9(g)] [but fails to show up in Figs. 9(a)–9(c) derived within a master-equation analysis]. In Fig. 11, we study this competition systematically using the results of our EOM analysis. In Fig. 11(a), we show the conductance at vanishing temperature $T \ll T_K$ as a function of the cavity level ϵ_c, corresponding to the green dashed line in Fig. 7(b). As the cavity level ϵ_c approaches ϵ_F, the formation of the molecular state suppresses the Kondo resonance peak; the latter reappears when the split cavity levels have crossed ϵ_F, resulting in a depression of the Kondo peak over a distance $\sim\Omega^2/U$. As the coupling Ω is decreased, the region where the Kondo peak is suppressed shrinks and vanishes in the limit $\Omega \to 0$.

As discussed above, Fermi-liquid theory provides us with an upper bound on the conductance that approximates well the true result at $\epsilon_c = 0$, i.e., at maximal depression. The crosses in Fig. 11 marking these Fermi-liquid bounds nearly coincide with the numerical results away from small couplings $\Omega/U > 0.01$, indicating that corrections by the leads become perturbative when the cavity becomes resonant and the dot-cavity singlet is formed. At small coupling Ω/U or at large cavity detuning ϵ_c, the violation of the Friedel sum rule by the EOM method becomes apparent as the conductance does not reach the unitary value $2e^2/\hbar$.

In Fig. 11(b), we keep the large dot-cavity coupling Ω from Fig. 11(a) and increase the temperature T instead. Again, the Kondo resonance is suppressed, while the singlet gap stays constant. As a result, the split cavity levels manifest themselves as pronounced cotunneling resonances. Choosing a configuration away from the particle-hole symmetric point results in an asymmetry between the two conductance peaks. The result of our equation-of-motion analysis is then in good agreement with the experimental data measured along the red dashed line in Fig. 9(g). Note the different widths of the conductance peaks along the source bias direction, the narrow Kondo peak of width T_K versus molecular singlet peaks extending over a region Γ_c.

[1]The expression for the exact Kondo temperature $T_K^{ex} = (U\Gamma/4)^{1/2}\exp[\pi\epsilon_d(\epsilon_d+U)/(\Gamma U)]$ can be found in Ref. [62] along with its derivation.

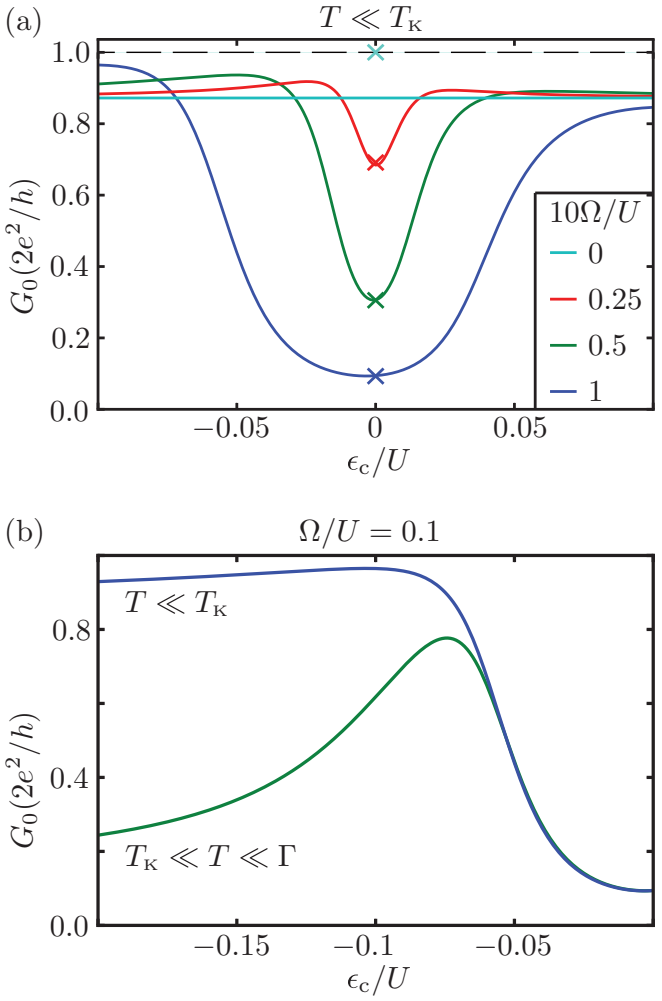

FIG. 11. Equilibrium conductance G_0 as a function of cavity-level position ϵ_c/U, corresponding to the green dashed line in Fig. 7(b) but for different couplings Ω/U and temperatures T/T_K, with $2\Gamma_L = 2\Gamma_R = 5\Gamma_c = \Gamma = U/10$ and $\epsilon_d/U = -\frac{2}{5}$. In (a), we show the conductance for very low temperatures $T \ll T_K$ and different coupling strengths Ω. The cavity suppresses the Kondo dot-lead singlet as the dot-cavity coupling is increased. The crosses correspond to the upper bounds given by the Fermi-liquid theory [60] and become exact in the limit where $\epsilon_d = -U/2$ [61]. In (b), we plot the strong-coupling $\Omega = 0.1\,U$, low-temperature transport [dark blue line in (a) and (b)] and the transport for the same coupling but at a temperature much larger than T_K (green line). We observe the disappearance of the Kondo conductance for a detuned cavity level $\epsilon_c \neq 0$. This unveils the cavity-assisted cotunneling features as the split cavity levels pass the Fermi level at $\epsilon_c \pm 6\alpha\Omega^2/U = 0$ [see Eq. (53)] (only one level shown here).

The combination of exact-diagonalization, master-equation, equation-of-motion, and Fermi-liquid-theory analyses therefore provides us with a complete and consistent understanding of transport across the dot-cavity system that is in agreement with the experimental findings. As a result, we conclude that the electrons in the dot-cavity hybrid indeed form an extended molecular singlet state that competes with the many-body Kondo singlet.

VII. SUMMARY AND OUTLOOK

Novel types of mesoscopic setups motivated, among other, by the prospects of quantum computing, combine various geometrical structures, including quantum channels, (multiple) dots, corrals, and cavities. Such structures define elementary building blocks of quantum engineering that can be combined into complex devices with specific functionalities. The coherent operation and coupling of these elements is a mandatory requirement for the operation of such devices. With the experiment in Ref. [23], an important step has been made in demonstrating spin-coherent operation of an electronic device involving a quantum dot coupled to an extended cavity of micrometer scale for the first time. This paper contributes a careful theoretical analysis of this experiment.

In our study, we first translated the experimental setup into a theoretical model. We have analyzed the single-particle transport properties of a cavity with electronic injection through a quantum point contact using the numerical package KWANT [29] (see Fig. 1). Combining our numerical findings with analytic results for the eigenstates of semicircular disks (Fig. 2) has led us to specific design principles for a cavity with separated sharp levels that are strongly coupled to the quantum point contact (see Fig. 3). The same methodology can serve as a test bed for a rapid and inexpensive optimization of new cavity designs, e.g., cavities connecting several quantum dots, thereby serving as a bus for the information transfer between qubits. In a subsequent step, we have constructed a model Hamiltonian that combines the single-particle properties of the cavity with the interacting physics of a quantum dot, thus defining an asymmetric artificial molecule, that is further coupled to leads in order to reproduce the transport geometry of the experimental setup [see Fig. 3(b)]. In constructing this model Hamiltonian, care has to be taken to avoid the appearance of Fano interference terms [34] that are not present in the experiment; within our formulation, the absence of such resonances is due to a phase averaging over the two-dimensional extent of the cavity (see Fig. 4).

Next, we have analyzed this model in three stages of increasing complexity: exact-diagonalization (ED), master-equation (ME), and equation-of-motion (EOM) approaches. Isolating the artificial molecule from the lead, the size of the involved Hilbert space became tractable and we could perform an ED study of the isolated dot-cavity system. We thus obtained ground-state and degeneracy maps which already match well the shape of the spectroscopic data provided by the experiment, confirming the validity of our dot-cavity molecular setup (see Figs. 7 and 8). In a second step, we have made use of the ED results in a master-equation approach [36–40]. We then obtained transport signatures that reproduce all the main features of the experiment, including the equilibrium and nonequilibrium transport data, ground-state maps, modulated Coulomb diamonds, and cavity-assisted cotunneling features in the blockaded region (see Figs. 7–9), with the exception of the zero-bias Kondo resonance. While the ME combined with the results from ED could capture the many-body physics of the dot-cavity system, it could not simultaneously deal with the many-body dot-lead physics responsible for the Kondo effect. We addressed this deficiency by applying an equation-of-motion analysis, using the method developed in

Refs. [47–49] enhanced by the presence of the cavity which enters the formalism through its contribution to the network self-energy (see Fig. 10). Once the dot Green's function has been found, the transport features could be calculated with the help of the Meir-Wingreen formula [50], finally allowing us to analyze the changeover from the Kondo dot-lead to the molecular dot-cavity singlet (see Fig. 11), and thus theoretically substantiating the main experimental claim of Ref. [23], the observation of spin-coherent transport across an extended quantum engineered system.

The setup discussed in this paper and further extensions thereof provide great opportunities for future research. Examples within the present dot-cavity system are the dependence of the molecular- to Kondo-singlet transition on disorder, magnetic field, or the level spacing in the cavity. On the theory side, it would be interesting to apply further, systematic methods to this problem such as the renormalization group (NRG and DMRG) [55–58] and the Bethe ansatz [63–65]. Most importantly, the ability to combine different functional elements opens the door for new designs and experiments. For example, it seems possible to use an electronic cavity as a "quantum bus" which connects distant qubits, allowing them to exchange quantum information through fully coherent operation. Another proposal is the study of two distant dots fused into an artificial molecule via a cavity. Such a device would give access to interesting Kondo physics involving a competition between several dots and leads, in particular, a superposition of two (macroscopic) Kondo clouds that may define a Kondo cat state.

ACKNOWLEDGMENTS

We thank E. van Nieuwenburg, T. Wolf, M. Goldstein, and R. Chitra for illuminating discussions and acknowledge financial support from the Swiss National Science Foundation, Division 2, and through the National Centre of Competence in Research "QSIT - Quantum Science and Technology".

M.S.F. and D.O. contributed equally to this work.

APPENDIX A: EXACT DIAGONALIZATION

To perform exact diagonalization for our dot-cavity system, we choose for each Fock space with particle numbers $\mathbf{N} = (N^\uparrow, N^\downarrow)_\sigma$ a basis

$$\left\{ |n_\mathrm{d}^\uparrow, n_\mathrm{d}^\downarrow, m_0^\uparrow, m_0^\downarrow, m_1^\uparrow, m_1^\downarrow, \ldots\rangle \middle| n_\mathrm{d}^\sigma + \sum_j m_j^\sigma = N^\sigma \right\}. \quad \text{(A1)}$$

Expressing the Hamiltonian H_dc (16) in this basis, we obtain a matrix $H_\mathrm{dc}^\mathbf{N}$. The diagonalization of this matrix provides us with the eigenenergies $\epsilon^\alpha_{N^\uparrow,N^\downarrow}$ and the eigenstates

$$|\psi^\alpha_{N^\uparrow,N^\downarrow}\rangle = \sum_{n_\mathrm{d}^\sigma + \sum_j m_j^\sigma = N^\sigma} \mathcal{C}^\alpha_{n_\mathrm{d}^\uparrow, n_\mathrm{d}^\downarrow, m_0^\uparrow, m_0^\downarrow, m_1^\uparrow, m_1^\downarrow, \ldots} \times |n_\mathrm{d}^\uparrow, n_\mathrm{d}^\downarrow, m_0^\uparrow, m_0^\downarrow, m_1^\uparrow, m_1^\downarrow, \ldots\rangle. \quad \text{(A2)}$$

As an example, we consider the case of a dot with a single level at ϵ_d and onsite interaction U, coupled via Ω to a single-cavity mode at ϵ_c. This case includes up to four particles and the basis vectors for the different Fock sectors are

$$\{|0,0,0,0\rangle\}, \quad \text{(A3)}$$

$$\{|1,0,0,0\rangle, |0,0,1,0\rangle, |0,1,0,0\rangle, |0,0,0,1\rangle\}, \quad \text{(A4)}$$

$$\left\{ |1,1,0,0\rangle, \frac{1}{\sqrt{2}}(|1,0,0,1\rangle + |0,1,1,0\rangle), |0,0,1,1\rangle, \frac{1}{\sqrt{2}}(|1,0,0,1\rangle - |0,1,1,0\rangle), |1,0,1,0\rangle, |0,1,0,1\rangle \right\}, \quad \text{(A5)}$$

$$\{|1,1,1,0\rangle, |1,0,1,1\rangle, |1,1,0,1\rangle, |0,1,1,1\rangle\}, \quad \text{(A6)}$$

$$\{|1,1,1,1\rangle\}, \quad \text{(A7)}$$

where we introduced a rotation in the two-particle Fock sector which simplifies the corresponding Hamiltonian. In this basis, the Hamiltonians become

$$H^0 = (0), \quad \text{(A8)}$$

$$H^1 = \begin{pmatrix} \epsilon_\mathrm{d} & \Omega \\ \Omega^* & \epsilon_\mathrm{c} \end{pmatrix} \otimes \begin{pmatrix} 1 & 0 \\ 0 & 1 \end{pmatrix}, \quad \text{(A9)}$$

$$H^2 = \begin{pmatrix} 2\epsilon_\mathrm{d} + U & \sqrt{2}\Omega & 0 & 0 \\ \sqrt{2}\Omega^* & \epsilon_\mathrm{d} + \epsilon_\mathrm{c} & \sqrt{2}\Omega & 0 \\ 0 & \sqrt{2}\Omega^* & 2\epsilon_\mathrm{c} & 0 \\ 0 & 0 & 0 & (\epsilon_\mathrm{c} + \epsilon_\mathrm{d})\mathbb{1}_3 \end{pmatrix}, \quad \text{(A10)}$$

$$H^3 = \begin{pmatrix} 2\epsilon_\mathrm{d} + U + \epsilon_\mathrm{c} & \Omega \\ \Omega^* & \epsilon_\mathrm{d} + 2\epsilon_\mathrm{c} \end{pmatrix} \otimes \begin{pmatrix} 1 & 0 \\ 0 & 1 \end{pmatrix}, \quad \text{(A11)}$$

$$H^4 = (2\epsilon_\mathrm{d} + 2\epsilon_\mathrm{c} + U), \quad \text{(A12)}$$

where we have maintained the ordering from the basis states above and $\mathbb{1}_3$ is the identity matrix in three dimensions such that H^2 spans the six-dimensional basis of the two-particle Fock sector. The gap opens in the Coulomb blockade region where the two-particle Fock sector ground state has a lower energy than the ground state of the one- and three-particle Fock sectors (see Fig. 6). In the region of interest $|\epsilon_\mathrm{c}| \ll U$, $\epsilon_\mathrm{d} \approx -U/2$, we can expand the ground-state energies of the one-, two-, and three-particle Fock sectors in Ω and ϵ_c to obtain

$$\epsilon_1^1 \approx \epsilon_\mathrm{d} - 2\frac{|\Omega|^2}{U}\frac{1}{1-\delta_{ph}}, \quad \text{(A13)}$$

$$\epsilon_2^1 \approx \epsilon_\mathrm{d} - 8\frac{|\Omega|^2}{U}\frac{1}{1-\delta_{ph}^2} + \epsilon_\mathrm{c}, \quad \text{(A14)}$$

$$\epsilon_3^1 \approx \epsilon_\mathrm{d} - 2\frac{|\Omega|^2}{U}\frac{1}{1+\delta_{ph}} + 2\epsilon_\mathrm{c}, \quad \text{(A15)}$$

where $\delta_{ph} = 1 + 2\epsilon_\mathrm{d}/U$ is the parameter which quantifies how far away from the particle-hole symmetric point $\delta_\mathrm{ph} = 0$ the dot is set. We then solve for the cavity-level position where the different Fock sectors are degenerate and obtain the conditions

$$\epsilon_\mathrm{c}^\pm = \pm\frac{6|\Omega|^2}{U}\left(\frac{1 \pm \delta_\mathrm{ph}/3}{1-\delta_\mathrm{ph}^2}\right) \quad \text{(A16)}$$

for the one- and two-particle, and the two- and three-particle Fock sectors being degenerate, respectively. This leads to

the minimal hybridization gap $12|\Omega|^2/U$ in the ground-state map. This gap diverges around the points $\epsilon_d = 0, U$ where the coupling Ω is no longer small compared to the energy difference between the basis states and the above nondegenerate perturbative approach is no longer valid. In this configuration, one obtains a gap of order Ω, the usual result of degenerate perturbation theory. We use the procedure outlined above to create the Hamiltonian matrices for larger systems and then diagonalize them numerically. We thus produce the eigenstates that we use to produce ground-state maps (Sec. IV) and that enter in the master equation (Sec. V).

APPENDIX B: MASTER-EQUATION APPROACH

The crucial ingredient of the master-equation approach are the rates (20) and (21) which we will derive in the following. The sequential tunneling transition rates $W^{\alpha,\alpha'}_{\mathbf{N},\mathbf{N}'}$ from a state $|\psi^{\alpha'}_{\mathbf{N}'}\rangle$ to state $|\psi^{\alpha}_{\mathbf{N}}\rangle$ are given by Fermi's golden rule [33]

$$W^{\alpha,\alpha'}_{\mathbf{N},\mathbf{N}'} = \frac{2\pi}{\hbar}\sum_{f,i}\left|\left\langle\psi^{\alpha}_{\mathbf{N}},\varphi_f\right|\bar{H}_{\rm tun}\left|\psi^{\alpha'}_{\mathbf{N}'},\varphi_i\right\rangle\right|^2 W_i\,\delta(E_f - E_i), \tag{B1}$$

with the notation $|\psi,\varphi\rangle = |\psi\rangle\otimes|\varphi\rangle$, where $|\varphi_i\rangle$ and $|\varphi_f\rangle$ represent the initial and final lead states, W_i is the probability for the lead to be in state $|\varphi_i\rangle$, and E_i and E_f correspond to the initial and final energies of the lead and molecular states. The tunneling Hamiltonian (11) consists of three parts: tunneling between the dot and the left lead, between the dot and the right lead, and between the cavity to the right lead. All of these processes have to be treated incoherently as discussed in Sec. III, thus giving rise to the rates

$$W^{\alpha,\alpha'}_{\mathbf{N},\mathbf{N}'} = W^{{\rm dL}\alpha,\alpha'}_{\mathbf{N},\mathbf{N}'} + W^{{\rm dR}\alpha,\alpha'}_{\mathbf{N},\mathbf{N}'} + W^{{\rm cR}\alpha,\alpha'}_{\mathbf{N},\mathbf{N}'}, \tag{B2}$$

where each term is given by an expression of the form of Eq. (B1) with the corresponding part of the tunneling Hamiltonian [see Eq. (11)]. The sequential tunneling rates only change the molecular occupation by one electron, i.e., $W^{\alpha,\alpha'}_{\mathbf{N}\pm\mathbf{e}_\sigma,\mathbf{N}} \neq 0$. For the rates, where the molecular occupation is increased from the left lead, the initial and final lead states differ by one electron in the left lead, i.e., $|\varphi_f\rangle = \sum_l c_{l\sigma}|\varphi_i\rangle$. Summing over all initial lead states, we obtain

$$\begin{aligned} W^{{\rm dL}\alpha,\alpha'}_{\mathbf{N}+\mathbf{e}_\sigma,\mathbf{N}} &= \frac{2\pi}{\hbar}\sum_l\left|\left\langle\psi^{\alpha}_{\mathbf{N}+\mathbf{e}_\sigma}\right|t_{\rm L}d^\dagger_\sigma\left|\psi^{\alpha'}_{\mathbf{N}}\right\rangle\right|^2 \\ &\quad\times n_{\rm F}(\epsilon_l-\mu_{\rm L})\delta\left(\epsilon^{\alpha}_{\mathbf{N}+\mathbf{e}_\sigma} - \epsilon_l - \epsilon^{\alpha'}_{\mathbf{N}}\right) \\ &= \frac{\Gamma_{\rm L}}{\hbar}\left|\left\langle\psi^{\alpha}_{\mathbf{N}+\mathbf{e}_\sigma}\right|d^\dagger_\sigma\left|\psi^{\alpha'}_{\mathbf{N}}\right\rangle\right|^2 n_{\rm F}\left(\epsilon^{\alpha}_{\mathbf{N}+\mathbf{e}_\sigma} - \epsilon^{\alpha'}_{\mathbf{N}} - \mu_{\rm L}\right), \end{aligned} \tag{B3}$$

where we used $\sum_i\langle\varphi_i|c^\dagger_{l\sigma}c_{l\sigma}|\varphi_i\rangle W_i = n_{\rm F}(\epsilon_l-\mu_{\rm L})$, replaced $\sum_l \to \int d\epsilon_l\rho_{\rm L}$, and made use of the definition of the rate $\Gamma_{\rm L} = 2\pi\rho_{\rm L}|t_{\rm L}|^2$. The rate $W^{{\rm dR}\alpha,\alpha'}_{\mathbf{N}+\mathbf{e}_\sigma,\mathbf{N}}$ follows analogously by replacing ${\rm L}\to{\rm R}$ in the expression above. The derivation of the rate $W^{{\rm cR}\alpha,\alpha'}_{\mathbf{N}+\mathbf{e}_\sigma,\mathbf{N}}$ follows the same arguments and the result is given by

$$\begin{aligned} W^{{\rm cR}\alpha,\alpha'}_{\mathbf{N}+\mathbf{e}_\sigma,\mathbf{N}} &= \frac{\Gamma_{\rm c}}{\hbar}\left|\left\langle\psi^{\alpha}_{\mathbf{N}+\mathbf{e}_\sigma}\right|\sum_j f^\dagger_{j\sigma}\left|\psi^{\alpha'}_{\mathbf{N}}\right\rangle\right|^2 n_{\rm F}(\epsilon^{\alpha}_{\mathbf{N}+\mathbf{e}_\sigma} - \epsilon^{\alpha'}_{\mathbf{N}} - \mu_{\rm R}) \\ &\approx \frac{\Gamma_{\rm c}}{\hbar}\sum_j\left|\left\langle\psi^{\alpha}_{\mathbf{N}+\mathbf{e}_\sigma}\right|f^\dagger_{j\sigma}\left|\psi^{\alpha'}_{\mathbf{N}}\right\rangle\right|^2 n_{\rm F}\left(\epsilon^{\alpha}_{\mathbf{N}+\mathbf{e}_\sigma} - \epsilon^{\alpha'}_{\mathbf{N}} - \mu_{\rm R}\right). \end{aligned} \tag{B4}$$

In the last step, we used the fact that the cavity-level spacing is large on the scale of temperature T; in this situation, interference terms involving different cavity levels are suppressed and we sum these processes incoherently. To calculate the rates which decrease the number of electrons on the artificial molecule, we make use of the relation $\sum_i\langle\varphi_i|c_{l\sigma}c^\dagger_{l\sigma}|\varphi_i\rangle W_i = 1 - n_{\rm F}(\epsilon_l-\mu_{\rm L})$ and obtain

$$W^{\rm da}_{\mathbf{N}-\mathbf{e}_\sigma,\mathbf{N}} = \tfrac{\Gamma_{\rm a}}{\hbar}\left|\left\langle\psi^{\alpha}_{\mathbf{N}-\mathbf{e}_\sigma}\right|d_\sigma\left|\psi^{\alpha'}_{\mathbf{N}}\right\rangle\right|^2\left[1 - n_{\rm F}\left(\epsilon^{\alpha'}_{\mathbf{N}} - \epsilon^{\alpha}_{\mathbf{N}-\mathbf{e}_\sigma} - \mu_{\rm a}\right)\right], \tag{B5}$$

$$\begin{aligned} W^{\rm cR}_{\mathbf{N}-\mathbf{e}_\sigma,\mathbf{N}} &= \frac{\Gamma_{\rm c}}{\hbar}\sum_j\left|\left\langle\psi^{\alpha}_{\mathbf{N}-\mathbf{e}_\sigma}\right|f_{j\sigma}\left|\psi^{\alpha'}_{\mathbf{N}}\right\rangle\right|^2 \\ &\quad\times\left[1 - n_{\rm F}\left(\epsilon^{\alpha'}_{\mathbf{N}} - \epsilon^{\alpha}_{\mathbf{N}-\mathbf{e}_\sigma} - \mu_{\rm R}\right)\right]. \end{aligned} \tag{B6}$$

The rates (B3)–(B6) constitute the main building blocks of our master-equation calculation. In determining these rates, we can apply the exact-diagonalization results by using the dot-cavity molecular spectrum $\epsilon^{\alpha}_{\mathbf{N}}$ as well as the associated eigenstates in the calculation of matrix elements of the type $\langle\psi^{\alpha}_{\mathbf{N}+\mathbf{e}_\sigma}|d^\dagger_\sigma|\psi^{\alpha'}_{\mathbf{N}}\rangle$ between different Fock states. We can thus produce the conductance maps in Figs. 7–9.

APPENDIX C: MEIR-WINGREEN FORMULA

The equation-of-motion method will provide us with the retarded Green's functions G_σ of the dot. We will show here that in equilibrium and at low temperatures $T \ll \Gamma$ this quantity is sufficient to calculate the conductance of the device. For a spin-independent tunneling, the Meir-Wingreen formula for the current from the dot to a lead a = L,R is given by [50]

$$I_{\rm a} = \frac{ie}{h}\sum_\sigma\int d\omega\,\Gamma_{\rm a}(\omega)[i\,n_{\rm F}(\omega-\mu_{\rm a}){\rm Im}G_\sigma(\omega) + G^<_\sigma(\omega)],$$

with the lesser Green's function $G^<_\sigma$ to be determined with the help of the Keldysh formalism [66]. We consider only a single-cavity level at $\epsilon_{\rm c}$ and drop the (artificial) Fano contribution to obtain the energy-dependent rates

$$\Gamma_{\rm L}(\omega) = \Gamma_{\rm L}, \tag{C1}$$

$$\Gamma_{\rm R}(\omega) = \Gamma_{\rm R} + \Gamma_{\rm c}\frac{|\Omega|^2}{(\epsilon_{\rm c}-\omega)^2 + \Gamma_{\rm c}^2/4}. \tag{C2}$$

Employing the symmetrization procedure of Ref. [50], we can rewrite the current through the dot in the form (we use that $I_{\rm L} = -I_{\rm R}$)

$$I = \frac{I_{\rm R}\Gamma_{\rm L} - I_{\rm L}\Gamma_{\rm R}(\epsilon_{\rm F})}{\Gamma_{\rm L} + \Gamma_{\rm R}(\epsilon_{\rm F})}. \tag{C3}$$

The contribution to the current I is limited to an energy window of extension T around the Fermi energy ϵ_F. Limiting ourselves to temperatures smaller than the tunneling rates divided be the derivative of the tunneling rates with respect to the energy $T\partial_\omega\Gamma_R \ll \Gamma_R$, the tunneling rate to the right lead is effectively constant, $\Gamma_R(\omega) \approx \Gamma_R(\epsilon_F = 0)$, and the symmetrization procedure of Ref. [50] can be carried through. As a result, we obtain an expression for the current that no longer depends on $G^<$,

$$I \approx \frac{2e}{h}\tilde{\Gamma}\sum_\sigma \int d\omega[n_F(\omega-\mu_L) - n_F(\omega-\mu_R)]\mathrm{Im}G_\sigma(\omega), \tag{C4}$$

with the rate

$$\tilde{\Gamma} = \frac{\Gamma_L\Gamma_R(\epsilon_F)}{\Gamma_L + \Gamma_R(\epsilon_F)}. \tag{C5}$$

Differentiating with respect to the bias voltage $V = -\mu_L/e$ and taking the equilibrium limit, we arrive at a formula which relates the conductance to the retarded Green's function of the dot

$$G_0 = \lim_{V\to 0}\frac{dI}{dV} \approx -\frac{2e^2}{h}\tilde{\Gamma}\sum_\sigma\int d\omega\,\frac{\beta\,\mathrm{Im}G_\sigma(\omega)}{4\,\cosh^2\frac{\beta\omega}{2}}. \tag{C6}$$

Combining this result with the equation-of-motion method described in Sec. VI, we can determine the conductance of the device including the Kondo effect.

APPENDIX D: EQUATION-OF-MOTION METHOD

In this appendix, we discuss some more technical aspects of the equation-of-motion method as found in the literature [47–49]. We start with the equations of motion for the required correlators and their truncation and then add some explanations on the derivation of the integral representations of the P and Q functions [Eqs. (42) and (43)].

Taking time derivatives on successive Green's functions, we obtain the following sets of equations of motion (after transformation to frequency space): the dot Green's function $\langle\langle d_\sigma; d_\sigma^\dagger\rangle\rangle$,

$$(z - e_d)\langle\langle d_\sigma; d_\sigma^\dagger\rangle\rangle = 1 + \sum_k t_k\langle\langle c_{k\sigma}; d_d^\dagger\rangle\rangle + U\langle\langle n_{\bar\sigma}d_\sigma; d_\sigma^\dagger\rangle\rangle, \tag{D1}$$

couples to the two-point correlator involving a lead electron

$$(z - \epsilon_k)\langle\langle c_{k\sigma}; d_d^\dagger\rangle\rangle = t_k^*\langle\langle d_\sigma; d_\sigma^\dagger\rangle\rangle, \tag{D2}$$

and to the four-point correlator with an additional particle on the dot

$$(z - \epsilon_d - U)\langle\langle n_{\bar\sigma}d_\sigma; d_\sigma^\dagger\rangle\rangle = \langle n_{\bar\sigma}\rangle + \sum_k[t_k\langle\langle n_{\bar\sigma}c_{k\sigma}; d_\sigma^\dagger\rangle\rangle + t_k\langle\langle d_{\bar\sigma}^\dagger c_{k\bar\sigma}d_\sigma; d_\sigma^\dagger\rangle\rangle - t_k^*\langle\langle c_{k\bar\sigma}^\dagger d_{\bar\sigma}d_\sigma; d_\sigma^\dagger\rangle\rangle]. \tag{D3}$$

The latter couples to further four-point correlators involving lead electrons,

$$(z - \epsilon_k)\langle\langle n_{\bar\sigma}c_{k\sigma}; d_\sigma^\dagger\rangle\rangle = t_k^*\langle\langle n_{\bar\sigma}d_\sigma; d_\sigma^\dagger\rangle\rangle + \sum_{k'}[t_{k'}\langle\langle d_{\bar\sigma}^\dagger c_{k'\bar\sigma}c_{k\sigma}; d_\sigma^\dagger\rangle\rangle - t_{k'}^*\langle\langle c_{k'\bar\sigma}^\dagger d_{\bar\sigma}c_{k\sigma}; d_\sigma^\dagger\rangle\rangle], \tag{D4}$$

$$(z - \epsilon_k)\langle\langle d_{\bar\sigma}^\dagger c_{k\bar\sigma}d_\sigma; d_\sigma^\dagger\rangle\rangle = \langle d_{\bar\sigma}^\dagger c_{k\bar\sigma}\rangle + t_k^*\langle\langle n_{\bar\sigma}d_\sigma; d_\sigma^\dagger\rangle\rangle + \sum_{k'}[t_{k'}\langle\langle d_{\bar\sigma}^\dagger c_{k\bar\sigma}c_{k'\sigma}; d_\sigma^\dagger\rangle\rangle - t_{k'}^*\langle\langle c_{k'\bar\sigma}^\dagger c_{k\bar\sigma}d_\sigma; d_\sigma^\dagger\rangle\rangle], \tag{D5}$$

$$(z - 2\epsilon_d - U + \epsilon_k)\langle\langle c_{k\bar\sigma}^\dagger d_{\bar\sigma}d_\sigma; d_\sigma^\dagger\rangle\rangle = \langle c_{k\bar\sigma}^\dagger d_{\bar\sigma}\rangle - t_k\langle\langle n_{\bar\sigma}d_\sigma; d_\sigma^\dagger\rangle\rangle + \sum_{k'}[t_{k'}\langle\langle c_{k\bar\sigma}^\dagger d_{\bar\sigma}c_{k'\sigma}; d_\sigma^\dagger\rangle\rangle + t_{k'}\langle\langle c_{k\bar\sigma}^\dagger c_{k'\bar\sigma}d_\sigma; d_\sigma^\dagger\rangle\rangle]. \tag{D6}$$

We truncate the sequence at the lowest level that includes the Kondo physics we are interested in. In decoupling the four-point correlators, we consistently decouple expressions with the same number of lead operators. This provides us with three truncation schemes: the mean-field zeroth-order $O(t^0)$ truncation

$$\langle\langle n_{\bar\sigma}d_\sigma; d_\sigma^\dagger\rangle\rangle \to \langle n_{\bar\sigma}\rangle\langle\langle d_\sigma; d_\sigma^\dagger\rangle\rangle, \tag{D7}$$

the $O(t)$ truncation

$$\langle\langle n_{\bar\sigma}c_{k\sigma}; d_\sigma^\dagger\rangle\rangle \to \langle n_{\bar\sigma}\rangle\langle\langle c_{k\sigma}; d_\sigma^\dagger\rangle\rangle, \tag{D8}$$

$$\langle\langle d_{\bar\sigma}^\dagger c_{k\bar\sigma}d_\sigma; d_\sigma^\dagger\rangle\rangle \to \langle d_{\bar\sigma}^\dagger c_{k\bar\sigma}\rangle\langle\langle d_\sigma; d_\sigma^\dagger\rangle\rangle, \tag{D9}$$

$$\langle\langle c_{k\bar\sigma}^\dagger d_{\bar\sigma}d_\sigma; d_\sigma^\dagger\rangle\rangle \to \langle c_{k\bar\sigma}^\dagger d_{\bar\sigma}\rangle\langle\langle d_\sigma; d_\sigma^\dagger\rangle\rangle, \tag{D10}$$

and finally the Lacroix $O(t^2)$ truncation

$$\langle\langle d_{\bar\sigma}^\dagger c_{k\bar\sigma}c_{k'\sigma}; d_\sigma^\dagger\rangle\rangle \to \langle d_{\bar\sigma}^\dagger c_{k\bar\sigma}\rangle\langle\langle c_{k'\sigma}; d_\sigma^\dagger\rangle\rangle, \tag{D11}$$

$$\langle\langle c_{k\bar\sigma}^\dagger d_{\bar\sigma}c_{k'\sigma}; d_\sigma^\dagger\rangle\rangle \to \langle c_{k\bar\sigma}^\dagger d_{\bar\sigma}\rangle\langle\langle c_{k'\sigma}; d_\sigma^\dagger\rangle\rangle, \tag{D12}$$

$$\langle\langle c_{k\bar\sigma}^\dagger c_{k'\bar\sigma}d_\sigma; d_\sigma^\dagger\rangle\rangle \to \langle c_{k\bar\sigma}^\dagger c_{k'\bar\sigma}\rangle\langle\langle d_\sigma; d_\sigma^\dagger\rangle\rangle. \tag{D13}$$

Note that all other decoupling terms vanish because the system Hamiltonian (8) is particle and spin conserving. We use the spectral theorem [see (34)] for general fermionic operators A and B to find the expectation values

$$\langle BA\rangle = \frac{i}{2\pi}\oint dz\, n_F(z)\langle\langle A; B\rangle\rangle. \tag{D14}$$

Combining the spectral theorem with the equations of motion (30), we immediately find that

$$t_k\langle d_{\bar\sigma}^\dagger c_{k\bar\sigma}\rangle = t_k^*\langle c_{k\bar\sigma}^\dagger d_{\bar\sigma}\rangle, \tag{D15}$$

which greatly simplifies the $O(t)$ truncation.

The functions P and Q [Eqs. (42) and (43)] can be brought into an integral form by using the spectral theorem (D14), the equation of motion (30), and some algebra:

$$\begin{aligned} P_\sigma(z) &\equiv \sum_k \frac{t_k\langle d_\sigma^\dagger c_{k\sigma}\rangle}{z-\epsilon_k} \\ &= \frac{i}{2\pi}\oint dz' n_{\rm F}(z')\sum_k \frac{t_k\langle\langle c_{k\sigma}; d_\sigma^\dagger\rangle\rangle_{z'}}{z-\epsilon_k} \\ &= \frac{i}{2\pi}\oint dz' n_{\rm F}(z')G_\sigma(z')\sum_k \frac{|t_k|^2}{(z-\epsilon_k)(z'-\epsilon_k)} \\ &= \frac{i}{2\pi}\oint dz' n_{\rm F}(z')G_\sigma(z')\frac{\Sigma(z')-\Sigma(z)}{z-z'}. \end{aligned} \tag{D16}$$

We find the analogous expression for $Q_\sigma(z)$,

$$\begin{aligned} Q_\sigma(z) &\equiv \sum_{kk'} \frac{t_{k'}t_k^*\langle c_{k\sigma}^\dagger c_{k'\sigma}\rangle}{z-\epsilon_{k'}} \\ &= \frac{i}{2\pi}\oint dz' n_{\rm F}(z')[1+\Sigma(z')G_\sigma(z')]\frac{\Sigma(z')-\Sigma(z)}{z-z'}, \end{aligned} \tag{D17}$$

by successively applying the two versions of the EOM (30) to the lead-lead correlator

$$\langle\langle c_{k'\sigma}; c_{k\sigma}^\dagger\rangle\rangle = \frac{\delta_{kk'}}{z-\epsilon_{k'}} + \frac{t_k t_{k'}^*}{(z-\epsilon_k)(z-\epsilon_{k'})}G_\sigma. \tag{D18}$$

When attempting to remove the spurious peak in the density of states in Lacroix truncation scheme one has to include a self-energy to the equation of motion (D4). This can be done rigorously as a further expansion in t^2, the so-called $O(t^4)$ truncation, yielding the self-energies to equations (D4)–(D6); details can be found in Refs. [48,49]. In Sec. VI we stay away from the dot particle-hole symmetric point ($\epsilon_{\rm d} \neq -U/2$) and thus avoid the anomaly.

APPENDIX E: NETWORK SELF-ENERGY

In any equation-of-motion method accounting for the lead states, the latter will appear explicitly only in the expression for the network self-energy, defined as the self-energy of the full Hamiltonian in the absence of the dot. Here, we show that the Hamiltonian with an energy-dependent tunneling to the right lead (3) and the Hamiltonian with discrete cavity levels (8) give rise to the same self-energy expression and are therefore equivalent in any truncation scheme that treats lead states on the same footing. The derivation of the self-energy is given in Ref. [47]. We focus first on our cavity model given by the Hamiltonian (8) with discrete cavity levels. We consider three independent contributions $\Sigma(z) = \Sigma_{\rm L}(z) + \Sigma_{\rm R}(z) + \Sigma_{\rm cav}(z)$, originating from the coupling to the source and drain lead $\Sigma_{\rm L}(z)$ and $\Sigma_{\rm R}(z)$, and to the cavity $\Sigma_{\rm cav}(z)$. The left and right leads are automatically independent, while the right lead and cavity contributions are treated such as not to include artificial Fano resonances (see Sec. III). With all microscopic quantities taken to be spin independent, so are the self-energies. The lead self-energies are given by $\Sigma_\alpha(z) = \sum_k |t_{\alpha k}|^2/(z-\epsilon_k)$, resulting in

$$\begin{aligned} \Sigma_\alpha(\omega \pm i\eta) &= \int d\omega' \frac{\rho_\alpha|t_\alpha|^2}{\omega-\omega'\pm i\eta} = \mp i\pi\rho_\alpha|t_\alpha|^2 \\ &\equiv \mp i\Gamma_\alpha/2, \end{aligned} \tag{E1}$$

and giving rise to an effective width $(\Gamma_{\rm L}+\Gamma_{\rm R})/2$ to the level. The cavity contribution is given by

$$\Sigma_{\rm cav}(z) = \sum_{j,l}\Omega_j^*[\mathcal{M}^{-1}(z)]_{jl}\Omega_l, \tag{E2}$$

with $\mathcal{M}_{jl}(z) = (z-\epsilon_{\rm c}^{(j)})\delta_{jl} - \tilde\Sigma_{jl}(z)$ the matrix which diagonalizes the right lead (excluding its coupling to the dot) (see the Appendix of Ref. [46]). Here, $\tilde\Sigma(z)$ is the self-energy resulting from the coupling of the cavity to the drain, in particular, the diagonal elements $\tilde\Sigma_{jj}(\omega\pm i\eta) = \mp i\Gamma_j/2 = \mp i\Gamma_{\rm c}/2$, where $\Gamma_{\rm c}$ is the rate defined in (13), give rise to a finite width of the cavity levels, while the off-diagonal elements $\tilde\Sigma_{jl}$ couple the different levels. Neglecting the coupling between the levels, $\tilde\Sigma_{jl} = 0$, a good approximation for $\delta_{\rm c} \gg \Gamma_j$, the inversion of $\mathcal{M}$ in (E2) becomes trivial and we obtain

$$\Sigma_{\rm cav}(\omega\pm i\eta) \approx \sum_j \frac{|\Omega_j|^2}{\omega-\epsilon_{\rm c}^{(j)}\pm i\Gamma_j/2}. \tag{E3}$$

Summing up all contributions, we obtain the network self-energy

$$\Sigma(\omega\pm i\eta) \approx \mp i(\Gamma_{\rm L}+\Gamma_{\rm R})/2 + \sum_j \frac{|\Omega_j|^2}{\omega-\epsilon_c^{(j)}\pm i\Gamma_j/2}. \tag{E4}$$

Let us shortly consider the self-energy originating from the original model (3), where it consists of two contributions $\Sigma(z) = \Sigma_{\rm L}(z) + \Sigma_{\rm R}(z)$ with $\Sigma_\alpha(z) = \sum_k |t_{\alpha k}|^2/(z-\epsilon_k)$. The contribution from the source lead is unchanged, i.e., $\Sigma_{\rm L}(\omega \pm i\eta) = \mp i\Gamma_{\rm L}/2$. For the right lead, using the energy dependent $t_{\rm R}(\omega)$ given in Eq. (7), the self-energy is given by the expression

$$\Sigma_{\rm R}(z) = \int d\omega' \frac{\rho_{\rm R}}{z-\omega'}\left|t_{\rm R} + \sum_j \frac{\lambda_j}{\omega'-\epsilon_{\rm c}^{(j)}+i\Gamma_j/2}\right|^2. \tag{E5}$$

Note that the interference of the first and second terms leads to Fano resonances, an artifact of the effective model (0D coupled to Fermi leads). We can easily avoid such terms by considering instead

$$\begin{aligned} \Sigma_{\rm R}(z) = &\int d\omega' \frac{\rho_{\rm R}}{z-\omega'}|t_{\rm R}|^2 \\ &+ \int d\omega' \frac{\rho_{\rm R}}{z-\omega'}\left|\sum_j \frac{\lambda_j}{\omega'-\epsilon_{\rm c}^{(j)}+i\Gamma_j/2}\right|^2, \end{aligned} \tag{E6}$$

where the first integral describes the unstructured lead, while the second one originates from the cavity. We consider the situation where the cavity-level separation is much larger than their width, i.e., $\delta_{\rm c} \gg \Gamma_j$, leading to the approximate

expression

$$\Sigma_{\mathrm{R}}(\omega \pm i\eta) \approx \int d\omega' \frac{\rho_{\mathrm{R}}}{\omega - \omega' \pm i\eta} |t_{\mathrm{R}}|^2 + \sum_j \int d\omega' \frac{\rho_{\mathrm{R}}}{\omega - \omega' \pm i\eta} \left| \frac{\lambda_j}{\omega' - \epsilon_{\mathrm{c}}^{(j)} + i\Gamma_j/2} \right|^2 = \mp i\Gamma_{\mathrm{R}}/2 + \sum_j \frac{2\pi\rho_{\mathrm{R}}|\lambda_j|^2/\Gamma_j}{\omega - \epsilon_{\mathrm{c}}^{(j)} \pm i\Gamma_j/2}. \quad \text{(E7)}$$

Comparing to the result in Eq. (E4), we see that the two expressions coincide if we relate the two models via $\lambda_j = \Omega_j t_j$. Hence, any EOM approach treating the cavity on the same level as the lead states will produce the same results for both our models. We use the self-energy derived in this appendix along with the EOM method from Sec. VI to solve for the Green's function of the dot self-consistently [see Eq. (45)]. The imaginary part ImG of these Green's functions is shown in Fig. 10 and appears indirectly through the Meir-Wingreen formula (see Appendix C) in Fig. 11.

[1] T. Ihn, *Semiconductor Nanostructures: Quantum States and Electronic Transport* (Oxford University Press, Oxford, 2010).
[2] L. P. Kouwenhoven, D. G. Austing, and S. Tarucha, Rep. Prog. Phys. **64**, 701 (2001).
[3] D. Goldhaber-Gordon, H. Shtrikman, D. Mahalu, D. Abusch-Magder, U. Meirav, and M. A. Kastner, Nature (London) **391**, 156 (1998).
[4] L. P. Kouwenhoven and L. Glazman, Phys. World **14**, 33 (2001).
[5] K. J. Thomas, J. T. Nicholls, M. Y. Simmons, M. Pepper, D. R. Mace, and D. A. Ritchie, Phys. Rev. Lett. **77**, 135 (1996).
[6] S. M. Cronenwett, H. J. Lynch, D. Goldhaber-Gordon, L. P. Kouwenhoven, C. M. Marcus, K. Hirose, N. S. Wingreen, and V. Umansky, Phys. Rev. Lett. **88**, 226805 (2002).
[7] K. Hirose, Y. Meir, and N. S. Wingreen, Phys. Rev. Lett. **90**, 026804 (2003).
[8] T. Rejec and Y. Meir, Nature (London) **442**, 900 (2006).
[9] R. de Picciotto, M. Reznikov, M. Heiblum, V. Umansky, G. Bunin, and D. Mahalu, Nature (London) **389**, 162 (1997).
[10] L. Saminadayar, D. C. Glattli, Y. Jin, and B. Etienne, Phys. Rev. Lett. **79**, 2526 (1997).
[11] M. Dolev, M. Heiblum, V. Umansky, A. Stern, and D. Mahalu, Nature (London) **452**, 829 (2008).
[12] J. A. Katine, M. A. Eriksson, A. S. Adourian, R. M. Westervelt, J. D. Edwards, A. Lupu-Sax, E. J. Heller, K. L. Campman, and A. C. Gossard, Phys. Rev. Lett. **79**, 4806 (1997).
[13] J. S. Hersch, M. R. Haggerty, and E. J. Heller, Phys. Rev. Lett. **83**, 5342 (1999).
[14] M. F. Crommie, C. P. Lutz, and D. M. Eigler, Nature (London) **363**, 524 (1993).
[15] H. C. Manoharan, C. P. Lutz, and D. M. Eigler, Nature (London) **403**, 512 (2000).
[16] O. Agam and A. Schiller, Phys. Rev. Lett. **86**, 484 (2001).
[17] G. A. Fiete and E. J. Heller, Rev. Mod. Phys. **75**, 933 (2003).
[18] N. J. Craig, J. M. Taylor, E. A. Lester, C. M. Marcus, M. P. Hanson, and A. C. Gossard, Science **304**, 565 (2004).
[19] R. M. Potok, I. G. Rau, H. Shtrikman, Y. Oreg, and D. Goldhaber-Gordon, Nature (London) **446**, 167 (2007).
[20] N. Roch, S. Florens, V. Bouchiat, W. Wernsdorfer, and F. Balestro, Nature (London) **453**, 633 (2008).
[21] T. Hayashi, T. Fujisawa, H. D. Cheong, Y. H. Jeong, and Y. Hirayama, Phys. Rev. Lett. **91**, 226804 (2003).
[22] J. R. Petta, A. C. Johnson, J. M. Taylor, E. A. Laird, A. Yacoby, M. D. Lukin, C. M. Marcus, M. P. Hanson, and A. C. Gossard, Science **309**, 2180 (2005).
[23] C. Rössler, D. Oehri, O. Zilberberg, G. Blatter, M. Karalic, J. Pijnenburg, A. Hofmann, T. Ihn, K. Ensslin, C. Reichl, and W. Wegscheider, Phys. Rev. Lett. **115**, 166603 (2015).
[24] S. Haroche, Rev. Mod. Phys. **85**, 1083 (2013).
[25] W. B. Thimm, J. Kroha, and J. von Delft, Phys. Rev. Lett. **82**, 2143 (1999).
[26] P. S. Cornaglia and C. A. Balseiro, Phys. Rev. B **66**, 174404 (2002).
[27] L. G. G. V. Dias da Silva, N. P. Sandler, K. Ingersent, and S. E. Ulloa, Phys. Rev. Lett. **97**, 096603 (2006).
[28] L. G. G. V. Dias da Silva, E. Vernek, K. Ingersent, N. Sandler, and S. E. Ulloa, Phys. Rev. B **87**, 205313 (2013).
[29] C. W. Groth, M. Wimmer, A. R. Akhmerov, and X. Waintal, New J. Phys. **16**, 063065 (2014).
[30] B. J. van Wees, H. van Houten, C. W. J. Beenakker, J. G. Williamson, L. P. Kouwenhoven, D. van der Marel, and C. T. Foxon, Phys. Rev. Lett. **60**, 848 (1988).
[31] D. A. Wharam, T. J. Thornton, R. Newbury, M. Pepper, H. Ahme, J. E. F. Frost, D. G. Hasko, D. C. Peacock, and D. A. Ritchie, J. Phys. C: Solid State Phys. **21**, L209 (1988).
[32] P. W. Anderson, Phys. Rev. **124**, 41 (1961).
[33] H. Bruus and K. Flensberg, *Many-body Quantum Theory in Condensed Matter Physics* (Oxford University Press, Oxford, 2004).
[34] U. Fano, Phys. Rev. **124**, 1866 (1961).
[35] Y. Alhassid, Rev. Mod. Phys **72**, 895 (2000).
[36] J. J. Sakurai and S. F. Tuan, *Modern Quantum Mechanics*, Vol. 1 (Addison-Wesley, Reading, MA, 1985).
[37] C. W. J. Beenakker, Phys. Rev. B **44**, 1646 (1991).
[38] A. N. Korotkov, Phys. Rev. B **49**, 10381 (1994).
[39] J. Koch, F. von Oppen, and A. V. Andreev, Phys. Rev. B **74**, 205438 (2006).
[40] J. Koch, Quantum transport through single-molecule devices, Ph.D. thesis, Freie Universität Berlin, 2006.
[41] M. S. Ferguson, C. Rössler, T. Ihn, K. Ensslin, G. Blatter, and O. Zilberberg, arXiv:1612.03850.
[42] A. Furusaki and K. A. Matveev, Phys. Rev. B **52**, 16676 (1995).
[43] D. M. Zumbühl, C. M. Marcus, M. P. Hanson, and A. C. Gossard, Phys. Rev. Lett. **93**, 256801 (2004).
[44] C. Lacroix, J. Phys. F: Met. Phys. **11**, 2389 (1981).
[45] C. Lacroix, J. Appl. Phys. **53**, 2131 (1982).
[46] O. Entin-Wohlman, A. Aharony, and Y. Meir, Phys. Rev. B **71**, 035333 (2005).
[47] V. Kashcheyevs, A. Aharony, and O. Entin-Wohlman, Phys. Rev. B **73**, 125338 (2006).

[48] R. Van Roermund, S.-y. Shiau, and M. Lavagna, Phys. Rev. B **81**, 165115 (2010).
[49] R. Van Roermund, Theoretical study of non-equilibrium transport in Kondo quantum dots, Ph.D. thesis, University of Grenoble, 2012.
[50] Y. Meir and N. S. Wingreen, Phys. Rev. Lett. **68**, 2512 (1992).
[51] D. N. Zubarev, Phys. Usp. **3**, 320 (1960).
[52] R. Kubo, J. Phys. Soc. Jpn. **17**, 1100 (1962).
[53] E. C. Goldberg, F. Flores, and R. C. Monreal, Phys. Rev. B **71**, 035112 (2005).
[54] R. C. Monreal and F. Flores, Phys. Rev. B **72**, 195105 (2005).
[55] K. G. Wilson, Rev. Mod. Phys. **47**, 773 (1975).
[56] R. Bulla, T. A. Costi, and T. Pruschke, Rev. Mod. Phys. **80**, 395 (2008).
[57] S. R. White, Phys. Rev. Lett. **69**, 2863 (1992).
[58] U. Schollwöck, Rev. Mod. Phys. **77**, 259 (2005).
[59] L. G. G. V. Dias da Silva, C. H. Lewenkopf, E. Vernek, G. J. Ferreira, and S. E. Ulloa, Phys. Rev. Lett. **119**, 116801 (2017).
[60] D. C. Langreth, Phys. Rev. **150**, 516 (1966).
[61] M. S. Ferguson, G. Blatter, and O. Zilberberg (unpublished).
[62] F. D. M. Haldane, Phys. Rev. Lett. **40**, 416 (1978).
[63] N. Andrei, Phys. Rev. Lett. **45**, 379 (1980).
[64] P. B. Wiegmann and A. M. Tsvelick, J. Phys. C: Solid State Phys. **16**, 2281 (1983).
[65] A. M. Tsvelick and P. B. Wiegmann, J. Phys. C: Solid State Phys. **16**, 2321 (1983).
[66] L. V. Keldysh, Zh. Eksp. Teor. Fiz. **47**, 1515 (1964) [Sov. Phys. JETP **20**, 1018 (1965)].